FDTD ANALYSIS OF METAMATERIAL COATED MICROWAVE ANTENNA

A Thesis

by

VIPIN KRISHNA REDDY CHOLLETI

Submitted to the Office of Graduate Studies of
Texas A&M University
in partial fulfillment of the requirements for the degree of

MASTER OF SCIENCE

May 2010

Major Subject: Electrical Engineering

FDTD ANALYSIS OF METAMATERIAL COATED MICROWAVE ANTENNA

A Thesis

by

VIPIN KRISHNA REDDY CHOLLETI

Submitted to the Office of Graduate Studies of
Texas A&M University
in partial fulfillment of the requirements for the degree of

MASTER OF SCIENCE

Approved by:

Chair of Committee,	Robert D. Nevels
Committee Members,	Kamran Entesari
	Gregory Huff
	Mary McDougall
Head of Department,	Costas N. Georghiades

May 2010

Major Subject: Electrical Engineering

ABSTRACT

FDTD Analysis of Metamaterial Coated Microwave Antenna. (May 2010)

Vipin Krishna Reddy Cholleti, B.Tech, Indian Institute of Technology Guwahati

Chair of Advisory Committee: Dr. Robert D. Nevels

Due to the growth in mobile wireless systems, electrically small antennas (ESAs), which are efficient and have significant bandwidth, are in great demand. But these requirements are contradictory. ESAs are known to be highly capacitive in nature. As a result of this, matching a power source to the ESA requires a matching network which increases the cost in terms of manufacturing as well as real estate. In recent years a new class of materials called metamaterials has emerged. These manmade materials with their unusual constitutive parameters possess immense potential to solve the problem of size reduction. This study seeks to validate, using Finite Difference Time Domain (FDTD) technique, a new metamaterial construct to achieve the desired objectives. FDTD code is developed for a cylindrical metamaterial wrapped around a modified biological antenna. The metamaterials are modeled using a Drude constitutive parameter model to simulate frequency dispersion. Epsilon Negative (ENG) as well as Double Negative (DNG) metamaterials are taken into consideration. Results show that the ESA using a metamaterial wraparound is found to have a quality factor lower than the theoretical Chu Limit. Both ENG as well as DNG metamaterials exhibit their potential. The resonant frequency of the metamaterial antenna is reduced over the classical design while the radiation pattern of the antenna remains virtually unchanged.

DEDICATION

The thesis is dedicated to my parents who emphasized the importance of education in one's life and helped me through all the rough and tumble times.

ACKNOWLEDGEMENTS

My deepest gratitude is to my advisor, Dr. Nevels. I have been amazingly fortunate to have an advisor who gave me the freedom to explore on my own and at the same time the guidance to recover when my steps faltered. His patience and support helped me overcome many crisis situations and finish this thesis. I hope that one day I would become as good an advisor to my students as Dr. Nevels has been to me.

I would like to thank my committee members, Dr. Entesari, Dr. Chan, Dr. Huff and Dr. McDougall for their guidance and support throughout the course of this research. Thanks also go to my friends and colleagues and the department faculty and staff for making my time at Texas A&M University a great experience. Finally, thanks to my family for their encouragement and love.

NOMENCLATURE

FDTD	Finite Difference Time Domain
c	Speed of Light in Vacuum
LHM	Left Handed Material
RHM	Right Handed Material
ESA	Electrically Small Antenna
Q	Quality Factor
ENG	Epsilon Negative
DNG	Double Negative
DPS	Double Positive
SRR	Split Ring Resonator

TABLE OF CONTENTS

CHAPTER Page

LIST OF FIGURES

FIGURE Page

FIGURE Page

LIST OF TABLES

CHAPTER I

INTRODUCTION

1.1 Introduction

Antennas which are electrically small, efficient and have significant bandwidth are in great demand. These requirements are contradictory. Electrically small antennas (ESAs) are known to be highly capacitive in nature. As a result of this matching a power source to the ESA requires a matching network which increases the cost both in terms of manufacturing expense as well as real estate. In recent years a new class of materials called metamaterials has emerged. These materials with their unusual constitutive parameters possess immense potential to solve the problem of size reduction. This study seeks to propose and validate a new metamaterial construct to achieve the desired objectives; electrically small, efficient, impedance matched and with reasonable bandwidth.

1.2 Thesis Outline

Chapter I provides an introduction to the thesis including the thesis outline. Chapter II introduces the procedure for applying finite-difference time domain (FDTD) method to time-domain Maxwell equations. Specifically the Yee's FDTD formulation is illustrated.

This thesis follows the style of *IEEE Transactions on Antennas and Propagation.*

In Chapter II the Yee FDTD scheme will be restricted to a model with linear, non-dispersive and non-magnetic dielectric. Three Dimensional as well as Two Dimensional computer implementations of FDTD will be explained. Various considerations such as numerical dispersion, stability, boundary conditions and Fourier transform implementation of the model are also discussed.

In Chapter III, a brief overview of metamaterials is provided. Some of the unique properties of metamaterials are discussed. FDTD formulation for metamaterials in a 2D rectangular coordinate system is also explained. To validate the FDTD code, a metamaterial slab is simulated to demonstrate the inverse Snell's law and show the refocusing of incident waves.

In Chapter IV limiting characteristics of ESAs are discussed. An ESA will be modeled using FDTD technique. The antenna design is discussed in a step by step manner and at each step FDTD is used to analyze the antenna. A modified version of the antenna is also simulated which will be used in Chapter V along with the metamaterial construct.

Chapter V provides a paradigm for achieving an efficient ESA. A metamaterial wrap is added around the modified antenna of Chapter IV. An FDTD code for cylindrical dispersive metamaterial is formulated. It is then used to discern the different properties of the metamaterial antenna. Use of Epsilon Negative (ENG) metamaterials and Double Negative (DNG) metamaterials is investigated. ESA-metamaterial system is shown to have a Q factor less than the Chu limit.

CHAPTER II

INTRODUCTION TO FINITE DIFFERENCE TIME DOMAIN METHOD

2.1 Introduction

In 1966 Kane Yee presented what we now refer to as the Finite-Difference Time-Domain (FDTD) [1] method for modeling electromagnetic phenomenon. The Yee's algorithm, as it is usually called in the literature, is well known for its robustness and versatility. The method approximates the differentiation operators of the Maxwell equations with finite-difference operators in time and space. It updates the Electric field (E) and Magnetic field (H) equations throughout the computational domain in terms of the past fields. The update equations are used in a leap-frog scheme to incrementally march Electric field (E) and Magnetic field (H) forward in time. After more than 30 years of development and improvement, the FDTD scheme has become well established and used widely in the modeling of all kinds of electromagnetic problems including propagation, scattering and radiation.

This chapter introduces the procedure for applying the FDTD method to time-domain Maxwell equations. Specifically the Yee's FDTD formulation will be illustrated. In this chapter the Yee FDTD scheme will be restricted to a model with a linear, non-dispersive and non-magnetic dielectric. Three Dimensional as well as Two Dimensional computer implementations of FDTD will be explained. Various considerations such as

numerical dispersion, stability, boundary conditions and Fourier transform implementation of the model will also be discussed.

2.2 Maxwell Equation

Generalized Maxwell's equations in time domain including magnetic current density and magnetic charge density are,

$$\nabla \times \vec{E} = -\vec{M} - \frac{\partial \vec{B}}{\partial t} \quad \text{(Faraday's Law)} \tag{2.2.1a}$$

$$\nabla \times \vec{H} = \vec{J} + \frac{\partial \vec{D}}{\partial t} \quad \text{(Ampere's Law)} \tag{2.2.1b}$$

$$\nabla \cdot \vec{D} = \rho_e \quad \text{(Gauss's Law for electric field)} \tag{2.2.1c}$$

$$\nabla \cdot \vec{E} = \rho_m \quad \text{(Gauss's Law for magnetic field)} \tag{2.2.1d}$$

The parameters for (2.2.1a)-(2.2.1d) are listed as follows:

$\vec{E}$ - Electric field intensity (volts/meter)

$\vec{H}$ - Magnetic field intensity (amperes/meter)

$\vec{D}$ - Electric flux density (coulombs/meter^2)

$\vec{B}$ - Magnetic flux density (webers/meter^2)

$\vec{J}$ - Electric current density (amperes/meter^2)

$\vec{M}$ - Magnetic current density (volts/meter^2)

ρ_e - Electric charge density (coulombs/meter^3)

ρ_m - Magnetic charge density (webers/meter^3)

In Linear, isotropic, non-dispersive materials (i.e., materials having field-independent, direction independent and frequency independent electric and magnetic properties), we can relate D to E and B to H using simple proportions:

$$\vec{\mathrm{D}} = \varepsilon_r \varepsilon_0 \vec{\mathrm{E}} = \varepsilon \vec{\mathrm{E}} \tag{2.2.2a}$$

$$\vec{\mathrm{B}} = \mu_r \mu_0 \vec{\mathrm{H}} = \mu \vec{\mathrm{H}} \tag{2.2.2b}$$

where,

ε_r - Relative electric permittivity (dimensionless)

ε_0 - Magnetic charge density (8.854×10^{-12} farads/meter)

μ_r - Relative magnetic permeability (dimensionless)

μ_0 - Free space magnetic permeability ($4\pi \times 10^{-7}$ henrys/meter)

Note that $\vec{\mathrm{J}}$ and $\vec{\mathrm{M}}$ account for independent sources as well as losses via conversion to heat energy. Therefore,

$$\vec{J} = \vec{J}_{source} + \sigma \vec{E} \tag{2.2.3a}$$

$$\vec{M} = \vec{M}_{source} + \sigma^* \vec{H} \tag{2.2.3b}$$

where,

σ - Electric conductivity (Siemens/meter)

σ^* - Magnetic conductivity (Ohms/meter)

2.3 FDTD Formulation and Algorithm Implementation

There are a number of finite-difference schemes for Maxwell's equations, but Yee scheme persists as it is very robust and versatile. The Yee algorithm solves for both electric and magnetic fields in time and space using the coupled Maxwell's curl equations, rather them solving each independently using wave equations. The solution is applicable for a wider class of structures and much more accurate. For simplicity, suppose the model is a three-dimensional (3D) model with linear, isotropic, non-dispersive dielectrics, and there are no electric and magnetic sources and magnetic losses are zero ($\vec{J}_{source} = 0, \vec{M}_{source} = 0, \sigma^* = 0$). From (2.2.1a), (2.2.1b),

$$\nabla \times \vec{H} = \sigma \vec{E} + \varepsilon \frac{\partial \vec{E}}{\partial t} \tag{2.3.1a}$$

$$\nabla \times \vec{E} = -\mu \frac{\partial \vec{H}}{\partial t} \tag{2.3.1b}$$

Equations (2.2.4a)-(2.2.4b) form the basis of Yee's FDTD scheme. Under Cartesian coordinate system, these can be further expanded as:

$$\frac{\partial H_x}{\partial t} = -\frac{1}{\mu}\left(\frac{\partial E_z}{\partial y} - \frac{\partial E_y}{\partial z}\right) \tag{2.3.2a}$$

$$\frac{\partial H_y}{\partial t} = -\frac{1}{\mu}\left(\frac{\partial E_x}{\partial z} - \frac{\partial E_z}{\partial x}\right) \tag{2.3.2b}$$

$$\frac{\partial H_z}{\partial t} = -\frac{1}{\mu}\left(\frac{\partial E_x}{\partial y} - \frac{\partial E_y}{\partial x}\right) \tag{2.3.2c}$$

$$\frac{\partial E_x}{\partial t} = -\frac{1}{\varepsilon}\left(\frac{\partial H_z}{\partial y} - \frac{\partial H_y}{\partial z} - \sigma E_x\right) \tag{2.3.2d}$$

$$\frac{\partial E_y}{\partial t} = -\frac{1}{\varepsilon}\left(\frac{\partial H_x}{\partial z} - \frac{\partial H_z}{\partial x} - \sigma E_y\right) \tag{2.3.2e}$$

$$\frac{\partial E_z}{\partial t} = -\frac{1}{\varepsilon}\left(\frac{\partial H_x}{\partial y} - \frac{\partial H_y}{\partial x} - \sigma E_z\right) \tag{2.3.2f}$$

Let us introduce the notation $E^n_{x(i,j,k)} = E_x(i\Delta x, j\Delta y, k\Delta z)$ and so on for E_y, E_z H_x, H_y and H_z components. In Yee's scheme, the model is first divided into many small cubes. The edges of each cube will form the three-dimensional space grid. The Yee's scheme can be generalized to variable cube size and non-orthogonal grid. The position of the E and field components in the space grid is shown in Figure 2.1.

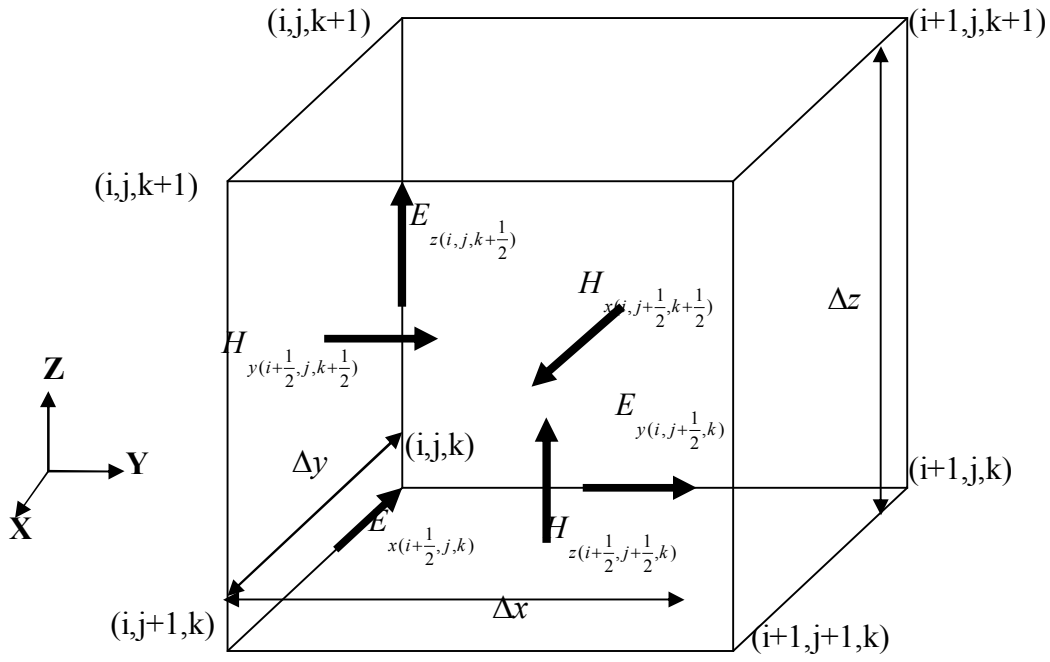

Figure 2.1: *Position of field components on the cube (i,j,k)*

The cube in Figure 2.1 is called the Yee Cell. From Figure 2.1, it is observed that each electric field component is surrounded by four magnetic field components and each magnetic field component is surrounded by four electric field components (If the field components on adjacent cubes are taken into account). For example, the component $H_{x(i,j+\frac{1}{2},k+\frac{1}{2})}$ is surrounded by $E_{z(i,j,k+\frac{1}{2})}$, $E_{z(i,j+1,k+\frac{1}{2})}$, $E_{y(i,j+\frac{1}{2},k)}$ and $E_{y(i,j+\frac{1}{2},k+1)}$. The inspiration for choosing this arrangement stems from the curl equations (2.3.1a)-(2.3.1b). As an example converting (2.3.1a) into integral form after using Stokes Theorem:

$$\oint_c \overline{E}.\overline{dl} = -\frac{\partial}{\partial t}\iint_s \overline{B}.\overline{ds} \tag{2.3.3}$$

This equation states that a changing magnetic flux will generate a circular electric field surrounding the 'flux tube'. Similarly the integral form of (2.3.1b) also states that a changing electric flux and an electric current will generate a circular magnetic field surrounding the 'flux tube'. Using the center difference operator to replace the time and space derivatives at time-step n and space lattice point $(i\Delta x,(j+\frac{1}{2})\Delta y,(k+\frac{1}{2})\Delta z)$ on (2.3.2a):

$$\frac{1}{\Delta t}(H^{n+\frac{1}{2}}_{x(i,j+\frac{1}{2},k+\frac{1}{2})} - H^{n-\frac{1}{2}}_{x(i,j+\frac{1}{2},k+\frac{1}{2})} = -\frac{1}{\mu}\left[\begin{array}{l}\frac{1}{\Delta y}\left(E^{n}_{z(i,j+1,k+\frac{1}{2})} - E^{n}_{z(i,j,k+\frac{1}{2})}\right) \\ -\frac{1}{\Delta z}\left(E^{n}_{y(i,j+\frac{1}{2},k+1)} - E^{n}_{y(i,j+\frac{1}{2},k)}\right)\end{array}\right] \tag{2.3.4}$$

$$\Rightarrow H^{n+\frac{1}{2}}_{x(i,j+\frac{1}{2},k+\frac{1}{2})} = H^{n-\frac{1}{2}}_{x(i,j+\frac{1}{2},k+\frac{1}{2})} - \frac{\Delta t}{\mu}\left[\begin{array}{l} \frac{1}{\Delta y}\left(E^{n}_{z(i,j+1,k+\frac{1}{2})} - E^{n}_{z(i,j,k+\frac{1}{2})} \right) \\ -\frac{1}{\Delta z}\left(E^{n}_{y(i,j+\frac{1}{2},k+1)} - E^{n}_{y(i,j+\frac{1}{2},k)} \right) \end{array}\right] \quad (2.3.5a)$$

Repeating the procedure for other field components,

$$H^{n+\frac{1}{2}}_{y(i+\frac{1}{2},j,k+\frac{1}{2})} = H^{n-\frac{1}{2}}_{y(i+\frac{1}{2},j,k+\frac{1}{2})} - \frac{\Delta t}{\mu}\left[\begin{array}{l} \frac{1}{\Delta z}\left(E^{n}_{x(i+\frac{1}{2},j,k+1)} - E^{n}_{x(i+\frac{1}{2},j,k)} \right) \\ -\frac{1}{\Delta x}\left(E^{n}_{z(i+1,j,k+\frac{1}{2})} - E^{n}_{z(i,j,k+\frac{1}{2})} \right) \end{array}\right] \quad (2.3.5b)$$

$$H^{n+\frac{1}{2}}_{z(i+\frac{1}{2},j+\frac{1}{2},k)} = H^{n-\frac{1}{2}}_{z(i+\frac{1}{2},j+\frac{1}{2},k)} - \frac{\Delta t}{\mu}\left[\begin{array}{l} \frac{1}{\Delta x}\left(E^{n}_{y(i,j+\frac{1}{2},k+1)} - E^{n}_{y(i,j+\frac{1}{2},k)} \right) \\ -\frac{1}{\Delta y}\left(E^{n}_{x(i+\frac{1}{2},j,k+1)} - E^{n}_{x(i+\frac{1}{2},j,k)} \right) \end{array}\right] \quad (2.3.5c)$$

$$E^{n+\frac{1}{2}}_{x(i+\frac{1}{2},j,k)} = \left(\frac{1-\frac{\sigma\Delta t}{2\varepsilon}}{1+\frac{\sigma\Delta t}{2\varepsilon}} \right) E^{n-\frac{1}{2}}_{x(i+\frac{1}{2},j,k)} - \frac{\frac{\sigma\Delta t}{2\varepsilon}}{1+\frac{\sigma\Delta t}{2\varepsilon}}\left[\begin{array}{l} \frac{1}{\Delta y}\left(H^{n+\frac{1}{2}}_{z(i+\frac{1}{2},j+\frac{1}{2},k)} - H^{n+\frac{1}{2}}_{z(i+\frac{1}{2},j-\frac{1}{2},k)} \right) \\ -\frac{1}{\Delta z}\left(H^{n+\frac{1}{2}}_{y(i+\frac{1}{2},j,k+\frac{1}{2})} - H^{n+\frac{1}{2}}_{y(i+\frac{1}{2},j,k-\frac{1}{2})} \right) \end{array}\right] \quad (2.3.5d)$$

$$E^{n+\frac{1}{2}}_{y(i,j+\frac{1}{2},k)} = \left(\frac{1-\frac{\sigma\Delta t}{2\varepsilon}}{1+\frac{\sigma\Delta t}{2\varepsilon}} \right) E^{n-\frac{1}{2}}_{y(i,j+\frac{1}{2},k)} - \frac{\frac{\sigma\Delta t}{2\varepsilon}}{1+\frac{\sigma\Delta t}{2\varepsilon}}\left[\begin{array}{l} \frac{1}{\Delta z}\left(H^{n+\frac{1}{2}}_{x(i,j+\frac{1}{2},k+\frac{1}{2})} - H^{n+\frac{1}{2}}_{x(i,j+\frac{1}{2},k-\frac{1}{2})} \right) \\ -\frac{1}{\Delta x}\left(H^{n+\frac{1}{2}}_{z(i+\frac{1}{2},j+\frac{1}{2},k)} - H^{n+\frac{1}{2}}_{z(i-\frac{1}{2},j+\frac{1}{2},k)} \right) \end{array}\right] \quad (2.3.5e)$$

$$E^{n+\frac{1}{2}}_{z(i,j,k+\frac{1}{2})} = \left(\frac{1-\frac{\sigma\Delta t}{2\varepsilon}}{1+\frac{\sigma\Delta t}{2\varepsilon}} \right) E^{n-\frac{1}{2}}_{z(i,j,k+\frac{1}{2})} - \frac{\frac{\sigma\Delta t}{2\varepsilon}}{1+\frac{\sigma\Delta t}{2\varepsilon}}\left[\begin{array}{l} \frac{1}{\Delta x}\left(H^{n+\frac{1}{2}}_{y(i+\frac{1}{2},j,k+\frac{1}{2})} - H^{n+\frac{1}{2}}_{y(i-\frac{1}{2},j,k+\frac{1}{2})} \right) \\ -\frac{1}{\Delta y}\left(H^{n+\frac{1}{2}}_{x(i,j+\frac{1}{2},k+\frac{1}{2})} - H^{n+\frac{1}{2}}_{x(i,j-\frac{1}{2},k+\frac{1}{2})} \right) \end{array}\right] \quad (2.3.5f)$$

Examination of (2.3.5a)-(2.3.5f) shows that all the field components fall on the locations accounted for by the space grid of Figure 2.1. Equations (2.3.5a)-(2.3.5f) are explicit in nature, thus computer implementation does not require solving a determinant or inverting a large matrix. To facilitate the implementation in digital computer, the indexes of the field components are renamed as shown in Figure 2.2, so that all the indexes become integers. This allows the value of each field component to be stored in a three-dimensional array in the software, where the array indexes correspond to the spatial indexes of Figure 2.2. In the figure additional field components are drawn to improve the clarity of the convention.

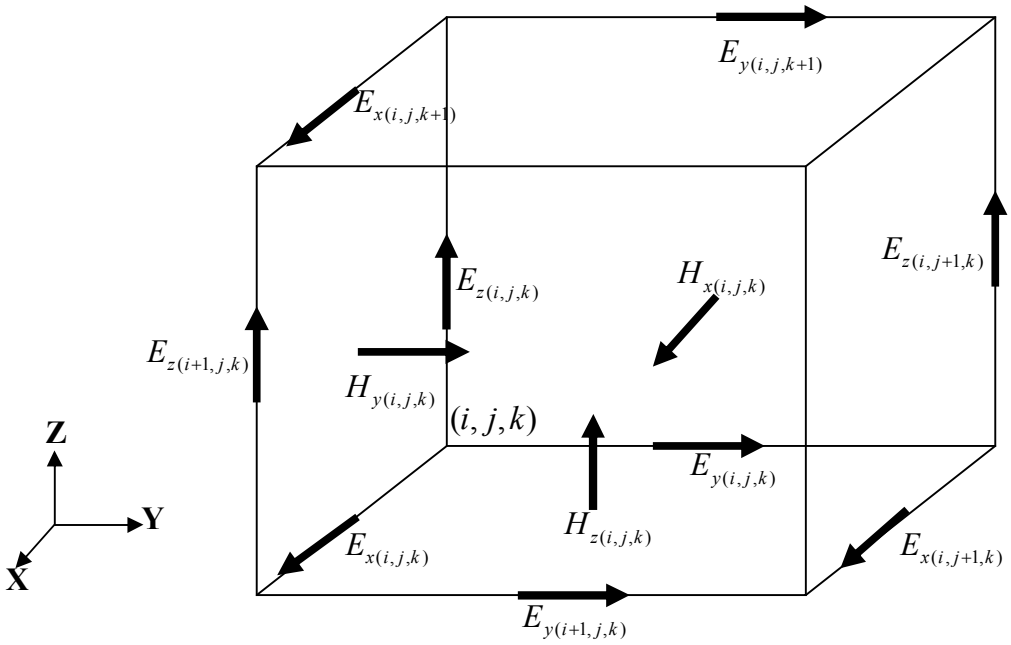

Figure 2.2: *Renaming the indexes of E and H field components corresponding to Cube (i,j,k)*

Using the new spatial indexes, the field components as in Figure 2.2, (2.3.3a)-(2.3.3f) become:

$$H_{x(i,j,k)}^{n+\frac{1}{2}} = H_{x(i,j,k)}^{n-\frac{1}{2}} - \frac{\Delta t}{\mu}\left[\begin{array}{l} \frac{1}{\Delta y}\left(E_{z(i,j+1,k)}^{n} - E_{z(i,j+1,k)}^{n}\right) \\ -\frac{1}{\Delta z}\left(E_{y(i,j,k+1)}^{n} - E_{y(i,j,k)}^{n}\right) \end{array}\right] \tag{2.3.6a}$$

$$H_{y(i,j,k)}^{n+\frac{1}{2}} = H_{y(i,j,k)}^{n-\frac{1}{2}} - \frac{\Delta t}{\mu}\left[\begin{array}{l} \frac{1}{\Delta z}\left(E_{x(i,j,k+1)}^{n} - E_{x(i,j,k)}^{n}\right) \\ -\frac{1}{\Delta x}\left(E_{z(i+1,j,k)}^{n} - E_{z(i,j,k)}^{n}\right) \end{array}\right] \tag{2.3.6a}$$

$$H_{z(i,j,k)}^{n+\frac{1}{2}} = H_{z(i,j,k)}^{n-\frac{1}{2}} - \frac{\Delta t}{\mu}\left[\begin{array}{l} \frac{1}{\Delta x}\left(E_{y(i,j,k+1)}^{n} - E_{y(i,j,k)}^{n}\right) \\ -\frac{1}{\Delta y}\left(E_{x(i,j,k+1)}^{n} - E_{x(i,j,k)}^{n}\right) \end{array}\right] \tag{2.3.6a}$$

$$E_{x(i,j,k)}^{n+\frac{1}{2}} = \left(\frac{1-\frac{\sigma\Delta t}{2\varepsilon}}{1+\frac{\sigma\Delta t}{2\varepsilon}}\right)E_{x(i,j,k)}^{n-\frac{1}{2}} - \frac{\frac{\sigma\Delta t}{2\varepsilon}}{1+\frac{\sigma\Delta t}{2\varepsilon}}\left[\begin{array}{l} \frac{1}{\Delta y}\left(H_{z(i,j,k)}^{n+\frac{1}{2}} - H_{z(i,j-1,k)}^{n+\frac{1}{2}}\right) \\ -\frac{1}{\Delta z}\left(H_{y(i,j,k)}^{n+\frac{1}{2}} - H_{y(i,j,k-1)}^{n+\frac{1}{2}}\right) \end{array}\right] \tag{2.3.6d}$$

$$E_{y(i,j,k)}^{n+\frac{1}{2}} = \left(\frac{1-\frac{\sigma\Delta t}{2\varepsilon}}{1+\frac{\sigma\Delta t}{2\varepsilon}}\right)E_{y(i,j,k)}^{n-\frac{1}{2}} - \frac{\frac{\sigma\Delta t}{2\varepsilon}}{1+\frac{\sigma\Delta t}{2\varepsilon}}\left[\begin{array}{l} \frac{1}{\Delta z}\left(H_{x(i,j,k)}^{n+\frac{1}{2}} - H_{x(i,j,k-1)}^{n+\frac{1}{2}}\right) \\ -\frac{1}{\Delta x}\left(H_{z(i,j,k)}^{n+\frac{1}{2}} - H_{z(i-1,j,k)}^{n+\frac{1}{2}}\right) \end{array}\right] \tag{2.3.6e}$$

$$E_{z(i,j,k)}^{n+\frac{1}{2}} = \left(\frac{1-\frac{\sigma\Delta t}{2\varepsilon}}{1+\frac{\sigma\Delta t}{2\varepsilon}}\right)E_{z(i,j,k)}^{n-\frac{1}{2}} - \frac{\frac{\sigma\Delta t}{2\varepsilon}}{1+\frac{\sigma\Delta t}{2\varepsilon}}\left[\begin{array}{l} \frac{1}{\Delta x}\left(H_{y(i,j,k)}^{n+\frac{1}{2}} - H_{y(i-1,j,k)}^{n+\frac{1}{2}}\right) \\ -\frac{1}{\Delta y}\left(H_{x(i,j,k)}^{n+\frac{1}{2}} - H_{x(i,j-1,k)}^{n+\frac{1}{2}}\right) \end{array}\right] \tag{2.3.6f}$$

Equations (2.3.6a)-(2.3.6f) form the basis of computer implementation of Yee's FDTD scheme for solving Maxwell's equations. Since (2.3.6a)-(2.3.6f) compute the new field components from the field components at previous time-steps, these equations are frequently called update equations. Notice that in the equations the temporal location of the E and H field components differs by half time-step ($\frac{1}{2}\Delta t$). In a typical simulation flow, one would determine the new H field components at n + $\frac{1}{2}$ from the previous field components using (2.3.6a)-(2.3.6c). Then the new E field components at n + 1 will be calculated using (2.3.6d)-(2.3.6f). The process is then repeated as many times as required until the last time-step is reached. Because of this, this scheme is sometimes called a "leapfrog scheme". The divergence equations (2.2.1c) and (2.2.1d) can be shown to be implicit in (2.3.6d)-(2.3.6f).

2.4 Reduction to Two Dimensions

Let neither the electromagnetic field excitation nor the modeled geometry have any variation in the z-direction. In effect, we assume that the partial derivative with respect to z on any of the field components is zero ($\frac{\partial}{\partial z} = 0$). Equations (2.3.6a)-(2.3.6f) can be written as:

$$H_{x(i,j,k)}^{n+\frac{1}{2}} = H_{x(i,j,k)}^{n-\frac{1}{2}} - \frac{\Delta t}{\mu}\left[\frac{1}{\Delta y}\left(E_{z(i,j+1,k)}^{n} - E_{z(i,j+1,k)}^{n}\right)\right] \qquad (2.4.1a)$$

$$H_{y(i,j,k)}^{n+\frac{1}{2}} = H_{y(i,j,k)}^{n-\frac{1}{2}} + \frac{\Delta t}{\mu}\left[\frac{1}{\Delta x}\left(E_{z(i+1,j,k)}^{n} - E_{z(i,j,k)}^{n}\right)\right] \qquad (2.\ 4.1b)$$

$$H_{z(i,j,k)}^{n+\frac{1}{2}} = H_{z(i,j,k)}^{n-\frac{1}{2}} - \frac{\Delta t}{\mu}\left[\begin{array}{l} \frac{1}{\Delta x}\left(E_{y(i,j,k+1)}^{n} - E_{y(i,j,k)}^{n}\right) \\ -\frac{1}{\Delta y}\left(E_{x(i,j,k+1)}^{n} - E_{x(i,j,k)}^{n}\right) \end{array}\right] \tag{2.4.1c}$$

$$E_{x(i,j,k)}^{n+\frac{1}{2}} = \left(\frac{1-\frac{\sigma\Delta t}{2\varepsilon}}{1+\frac{\sigma\Delta t}{2\varepsilon}}\right) E_{x(i,j,k)}^{n-\frac{1}{2}} - \frac{\frac{\sigma\Delta t}{2\varepsilon}}{1+\frac{\sigma\Delta t}{2\varepsilon}}\left[\frac{1}{\Delta y}\left(H_{z(i,j,k)}^{n+\frac{1}{2}} - H_{z(i,j-1,k)}^{n+\frac{1}{2}}\right)\right] \tag{2.4.1d}$$

$$E_{y(i,j,k)}^{n+\frac{1}{2}} = \left(\frac{1-\frac{\sigma\Delta t}{2\varepsilon}}{1+\frac{\sigma\Delta t}{2\varepsilon}}\right) E_{y(i,j,k)}^{n-\frac{1}{2}} + \frac{\frac{\sigma\Delta t}{2\varepsilon}}{1+\frac{\sigma\Delta t}{2\varepsilon}}\left[\frac{1}{\Delta x}\left(H_{z(i,j,k)}^{n+\frac{1}{2}} - H_{z(i-1,j,k)}^{n+\frac{1}{2}}\right)\right] \tag{2.4.1e}$$

$$E_{z(i,j,k)}^{n+\frac{1}{2}} = \left(\frac{1-\frac{\sigma\Delta t}{2\varepsilon}}{1+\frac{\sigma\Delta t}{2\varepsilon}}\right) E_{z(i,j,k)}^{n-\frac{1}{2}} - \frac{\frac{\sigma\Delta t}{2\varepsilon}}{1+\frac{\sigma\Delta t}{2\varepsilon}}\left[\begin{array}{l} \frac{1}{\Delta x}\left(H_{y(i,j,k)}^{n+\frac{1}{2}} - H_{y(i-1,j,k)}^{n+\frac{1}{2}}\right) \\ -\frac{1}{\Delta y}\left(H_{x(i,j,k)}^{n+\frac{1}{2}} - H_{x(i,j-1,k)}^{n+\frac{1}{2}}\right) \end{array}\right] \tag{2.4.1f}$$

Equations (2.4.1a)-(2.4.1f) when uncoupled can be separated into Transverse Magnetic (TM) and Transverse Electric (TE) modes.

2.5 Numerical Dispersion

The numerical algorithms for Maxwell's curl equations as defined by (2.3.6a)-(2.3.6f) causes dispersion in the simulated wave modes in the computational domain. For instance in vacuum, the phase velocity of the numerical wave modes in the FDTD grid can differ from vacuum speed of light. In fact the phase velocity of the numerical wave modes is a function of wavelength, the direction of propagation and the size of the cubes. This numerical dispersion can lead to nonphysical results such as broadening and ringing

of single-pulse waveforms, imprecise cancelation of multiple scattered waves and pseudo refraction. A detailed analysis of this numerical dispersion is presented in Chapter V of Taflove [2] and consequently will not be discussed here. It is shown in [1, 2] that to limit the amount of numerical dispersion, the edges of each cube must be at least ten times smaller than the shortest wavelength expected to propagate in the computational domain. Of course the numerical dispersion will be suppressed even further if a smaller cube size is chosen. However using a cube size that is too small will increase the number of cubes needed to fill the computational domain and hence increase computational resource demand of the model. The rule-of-thumb of $\Delta x, \Delta y, \Delta z \le \frac{\lambda_0}{10}$ where λ_0 is the wavelength corresponding to the expected highest significant harmonics in the model is adequate for most purposes. For 1D FDTD, if one chooses $\Delta t = \frac{\Delta x}{c}$, there will be no numerical dispersion regardless of the choice of Δx. This is called the 'magic time step'. There is no 'magic time step' for 2D and 3D cases.

2.6 Numerical Stability

The numerical algorithm for Maxwell's curl equations as defined by (2.3.6a)-(2.3.6f) requires that the time increment Δt have a specific bound relative to the spatial discretization ($\Delta x, \Delta y$, Δz). For an isotropic FDTD analysis based on central differencing to remain stable the following mathematical statement must be true*;*

$$\Delta t \le c \sqrt{\frac{1}{(\Delta x)^2} + \frac{1}{(\Delta y)^2} + \frac{1}{(\Delta z)^2}} \qquad (2.6.1)$$

where, c is the velocity of light in free space.

$$\Delta x = \Delta y = \Delta z = \delta \quad \Rightarrow \quad \Delta t \leq \frac{\delta}{c\sqrt{3}} \tag{2.6.2}$$

Equation (2.6.1) is known as Comant-Freidrichs-Lewy (CFL) Stability Criterion. In an unstable model the computed result for E and H field components will increase without limit as the simulation progresses.

2.7 Sources

To simulate a voltage source excitation, it is necessary to impose an electric field in a computational grid. Sources are characterized according to their shape or FDTD implementation.

2.7.1 Gaussian and Sinusoid Source

A source can either be sinusoidal or a Gaussian pulse. A Gaussian pulse is desirable as the excitation because its frequency spectrum is also Gaussian and will provide frequency-domain information from dc to the highest frequency that will propagate in the numerical lattice. Ramped Sinusoid is particularly useful for visualizing field interactions. Figure 2.3(a) and (b) show the Gaussian pulse and ramped sinusoid of frequency 20 GHz along with their frequency spectrum respectively.

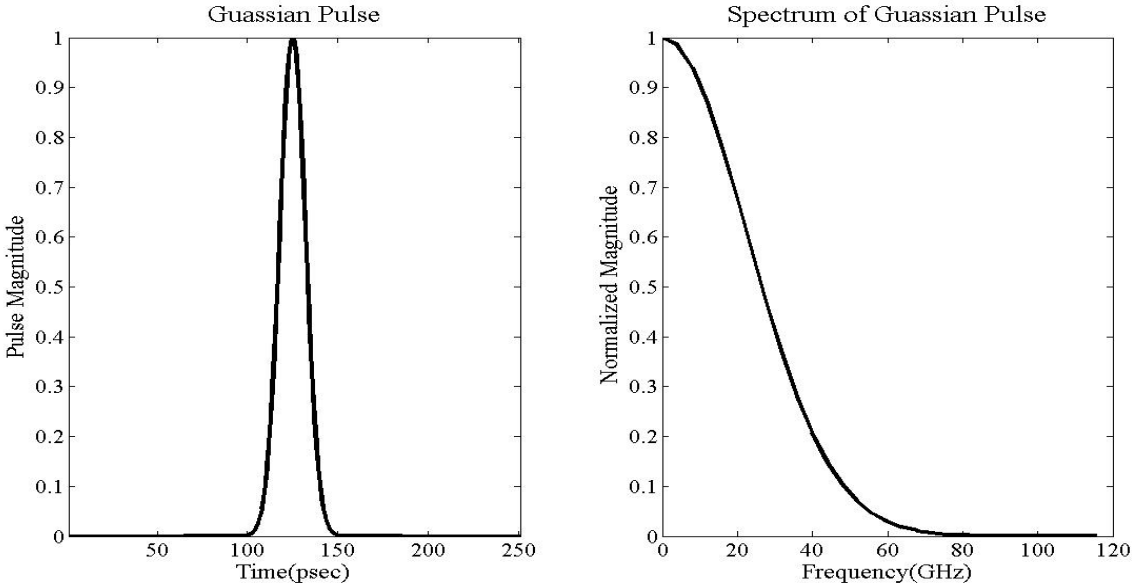

Figure 2.3(a): *Gaussian Pulse along with its frequency spectrum*

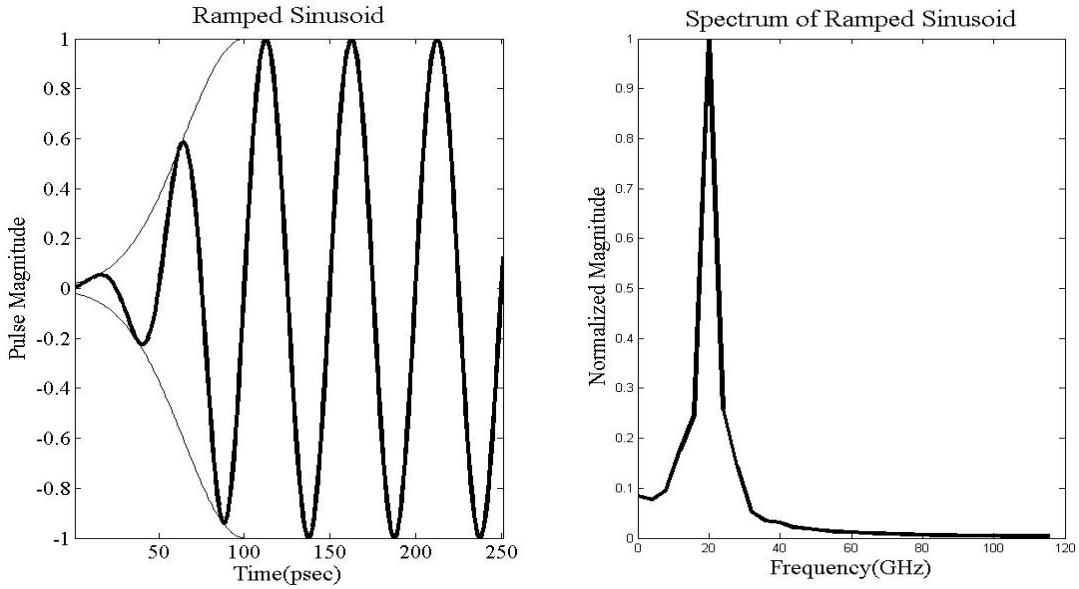

Figure 2.3(b): *Ramped Sinusoid along with its frequency spectrum*

In discrete form the Gaussian time pulse is given by,

$$g(n\Delta t) = e^{-\frac{(n\Delta t - n_0\Delta t)^2}{(\beta\Delta t)^2}} \qquad (2.7.1.1)$$

where n is the time increment and n_0 is the number of time increments it takes for the pulse to reach its peak value. A 'rule of thumb' for choosing n_0 is that at the 'turn on' time (n = 0) the Gaussian time function should be down ~140dB.

2.7.2 Hard and Soft Source

There are two types of sources depending on computer implementation, the Hard Source and the Soft Source. If a source is assigned a fixed E-field, it is referred to as hard source. If a propagating wave value is added to E-field at a certain point, it is referred to as soft source. With a hard source, a propagating wave will be reflected from source point, which appears to be a conducting wall to the incoming wave, but a soft source will allow the propagating wave to pass through. A soft source is modeled as,

$$E_z^n\Big|_{i_s}^{n+1} = E_{source}\Big|^{n+\frac{1}{2}} + E_z^n\Big|_{i_s}^{n+1} + \frac{\Delta t}{\varepsilon\Delta x}\left(H_y\Big|_{i_s+\frac{1}{2}}^{n+1} - H_y\Big|_{i_s-\frac{1}{2}}^{n+1} \right) \qquad (2.7.2.1a)$$

A hard source is modeled as,

$$E_z^n\Big|_{i_s}^{n+1} = E_{source}\Big|^{n+\frac{1}{2}} \qquad (2.7.2.1b)$$

2.8 Frequency Domain Analysis

The FDTD method is conducted in the time domain. In order to obtain frequency domain characteristics such as scattering parameters, reflection coefficients and input

impedance, Fourier Transform is used to post process the results. The Fourier transform of an electric field E(t) at frequency f = f_k is calculated by,

$$e(f_k) = \int_{-\infty}^{\infty} E(t) e^{-j2\pi f_k t} dt \tag{2.8.1}$$

Discretizing this equation, the N point Discrete Fourier Transform (DFT) is given by,

$$e(f_k) = \Delta t \sum_{n=0}^{N-1} E(n\Delta t) e^{-j2\pi f_k \Delta t} \tag{2.8.2}$$

The DFT does not require the storage of large data sets as it can be implemented on the fly by choosing in advance at which frequency we want the system response. The reflection coefficient is given by,

$$\Gamma(f_k) = \frac{\left| DFT_{f_k}(E^{total}_{i,j,k} - E^{inc}_{i,j,k}) \right|}{\left| DFT_{f_k}(E^{inc}_{i,j,k}) \right|} \tag{2.8.3}$$

2.9 Boundary Conditions

In order to analyze Electromagnetic interactions in unbounded media, one must truncate the mesh in such a way that the exterior boundary looks like an unbounded medium. Various Boundary conditions are available like Engquist-Majda[3], Mur[4], Liao[5], Perfectly matched layer[6] to name a few. A perfectly matched layer boundary condition will be implemented in Chapter II and Liao boundary condition will be used in Chapter III.

2.10 Implementation of Basic FDTD Algorithm

Figure 2.4 shows the flow chart for the implementation FDTD Algorithm.

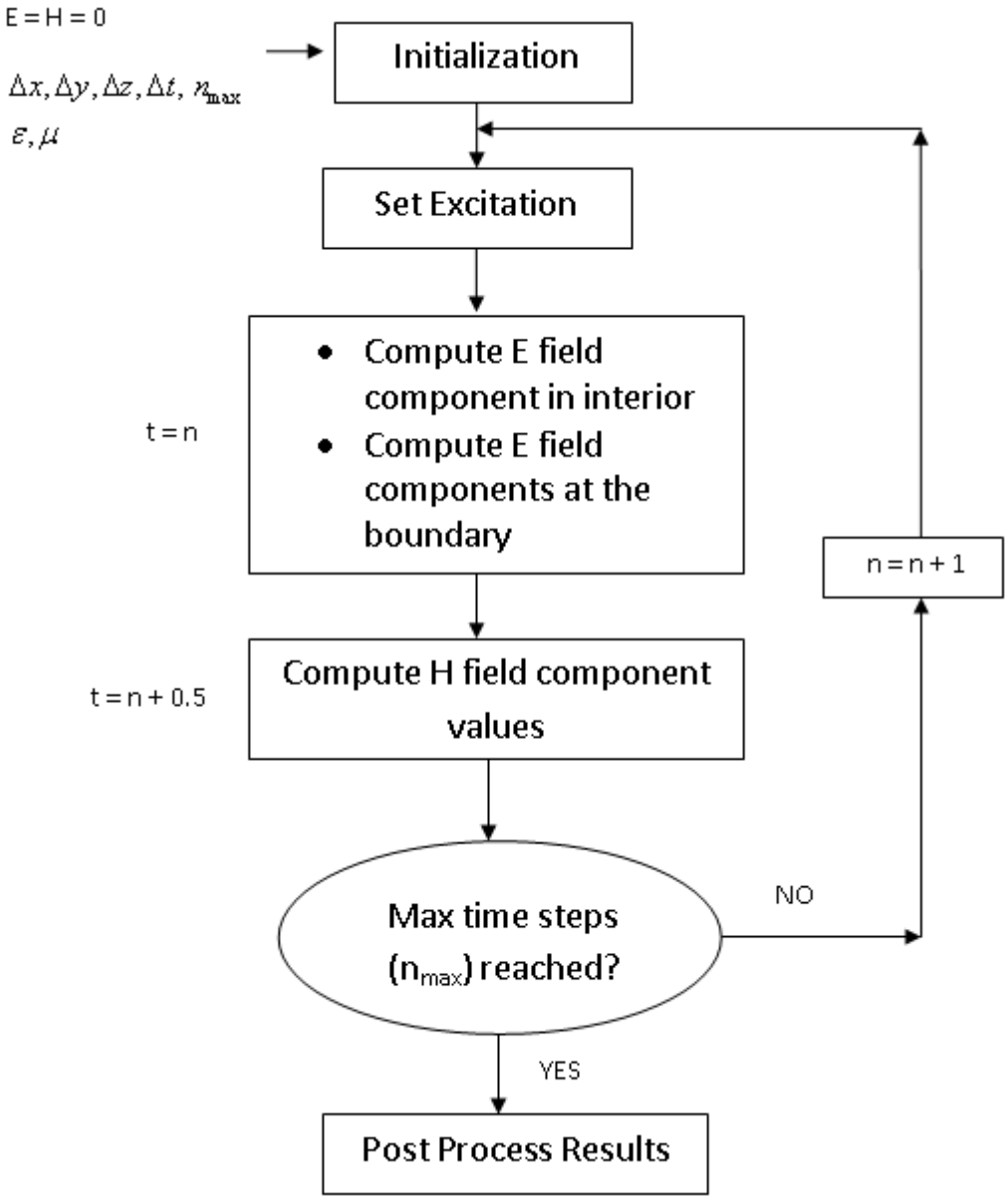

Figure 2.4: *FDTD Algorithm flow chart*

2.10 Summary

In this chapter, the fundamental issues regarding the original Yee FDTD algorithm were introduced and the algorithm implementation discussed. Several key aspects of the FDTD algorithm like dispersion, stability, sources and boundary conditions have also been dealt in a brief manner.

CHAPTER III

METAMATERIALS AND DISPERSIVE FDTD

3.1 Introduction

Over the last decades, a new class of artificially created materials, known as electromagnetic metamaterials [7-8] or simply metamaterials, has received considerable attention both in the physics and engineering communities. Metamaterials can offer electromagnetic properties that are difficult or impossible to achieve with conventional, naturally occurring materials. A medium of this type is called "Left-handed Metamaterial" (LHM), a term first applied by Veselago in 1968 [9] because the wave vector, electric field vector, and magnetic field vector form a left-handed system. In his pioneering work, Veselago pointed out that LHMs have simultaneously negative permittivity and permeability and some unique properties, such as inverse Snell effect, an inverse Doppler shift and backwards-directed Cherenkov radiation. In 1999, Pendry et al [8] demonstrated that materials with an array of split ring resonators (SRRs) produce negative permeability over certain frequency bands. Combining a two-dimensional (2D) array of SRRs interspersed with a 2D array of metallic wires, to give negative permittivity, enabled the construction of LHMs with both effective permittivity and permeability negative. In 2001, Smith et al [7] demonstrated for the first time the experimental existence of LHMs.

In this chapter, a brief overview of metamaterials is provided. Some of the unique properties of metamaterials are discussed. An FDTD formulation for

metamaterials in a 2D rectangular coordinate system is provided for numerically simulating these structures. To validate the FDTD code, a metamaterial slab is simulated to demonstrate the inverse Snell's law discussed in section 3.3 of the thesis and show the refocusing of incident waves.

3.2 Electromagnetic Metamaterials

Metamaterials are engineered materials which can be either composites or combination of electrical and magnetic elements (eg. split rings and wires) that exhibit superior properties not found in nature and are not observed in the constituent materials. Almost all natural materials follow the so called right-hand rule because their permeability (μ) and permittivity (ε) both have positive signs. Such materials are referred to as Right Handed materials (RHM). The electric field ($\vec{E}$), magnetic field ($\vec{H}$) and wave vector ($\vec{k}$) in such materials form a right handed set of vectors as shown in Figure 3.1(a), wherein $\vec{E}$ is along the $+x$ direction, $\vec{H}$ is along the $+y$ direction and the wave propagates along $+z$ direction, and thus $\vec{E}$, $\vec{H}$ and $\vec{k}$ build a right-handed triplet. All materials encountered so far in a natural form are RHM. In LHM, $\vec{k}$ is reversed in comparison with what it should have been for a RHM, $\vec{E}$ and $\vec{H}$ make a left-handed triplet with $\vec{k}$. That means that if $\vec{E}$ is along $+x$ direction and $\vec{H}$ is along the $+y$ direction, the wave will propagate along the $-z$ direction in LHM as shown in Figure 3.1(b).

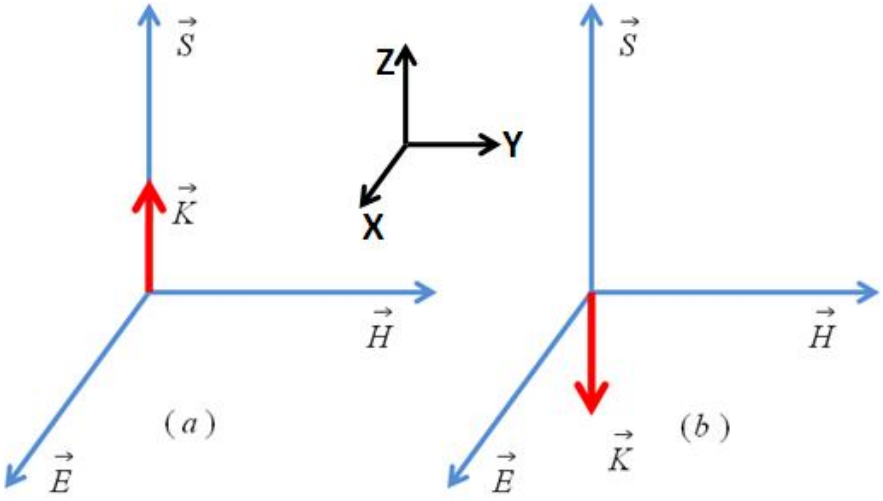

Figure 3.1(a) *Right handed triplet for normal materials and* (b) *Left handed triplet for metamaterials*

Now, examine the direction of the energy flow in LHM, which is characterized by the Poynting Vector ($\vec{S}$) as follows,

$$\vec{S} = \frac{c}{4\pi}\vec{E}\times\vec{H} \tag{3.2.1}$$

The Poynting vector power density can be written as:

$$\vec{E}\times\vec{H} = \frac{1}{\omega^2\mu\varepsilon}\left(\vec{k}\times\vec{E}\right)\times\left(\vec{k}\times\vec{H}\right) \tag{3.2.2a}$$

$$= \frac{1}{\omega\sqrt{\mu\varepsilon}}\left(\vec{k}\times\vec{E}\right)\times\vec{E} = \frac{-\vec{k}}{\omega\sqrt{\mu\varepsilon}}\left|\vec{E}\right|^2 \tag{3.2.2b}$$

$$= \frac{-1}{\omega\sqrt{\mu\varepsilon}}\vec{H}\times\left(\vec{k}\times\vec{H}\right) = \frac{-\vec{k}}{\omega\sqrt{\mu\varepsilon}}\left|\vec{H}\right|^2 \tag{3.2.2c}$$

In a RHM ($\varepsilon > 0$ and $\mu > 0$), the Poynting vector $\vec{S}$ is in the same direction as $\vec{k}$ as shown in Figure 1.1, wherein both $\vec{S}$ and $\vec{k}$ are along the +*z* direction. For LHM ($\varepsilon < 0$ and $\mu < 0$), $\vec{k}$ is along the -*z* direction as shown in Figure 1.2. As derived in equations (3.2.2b) and (3.2.2c), the Poynting vector $\vec{S}$ is in the opposite direction of $\vec{k}$ for ($\varepsilon < 0$ and $\mu < 0$). Thus $\vec{S}$ is in the opposite direction of $\vec{k}$ and along the +*z* direction as shown in Figure 3.1(b). Consequently, the energy flow and the phase velocity in LHM are in opposite directions.

3.3 Unique Properties of LHMs

- **Negative Refractive Index:** A conventional material with $\varepsilon_r > 0$ and $\mu_r > 0$ has a refractive index is given by $n = \sqrt{\varepsilon_r \mu_r}$, and therefore possesses a positive refractive index. A LHM has both negative permittivity ($\varepsilon_r(\omega) < 0$) and negative permeability ($\mu_r(\omega) < 0$), and hence the refractive index *n* has negative value.

- **Inverse Snell's Law:** An incident light that enters LHMs from a right-handed medium will undergo refraction, but opposite to that usually observed for two right-handed media. Snell's law is described as:

$$\frac{\sin(\theta_i)}{\sin(\theta_r)} = \frac{n_2}{n_1} \tag{3.3.1}$$

where θ_i is the incident angle, θ_r is the refraction angle, n_1 is the refractive index for the incident medium and n_2 is the refractive index for transmitted medium.

- **Negative Phase Velocity:** The phase velocity expression $v_p = \frac{c}{n(\omega)}$ shows that the phase velocity v_p is inversely related to the index of refraction $n(\omega)$, here c denotes the speed of light in a vacuum. A LHM has a negative refractive index ($n(\omega) < 0$), and therefore the phase velocity has a negative value. In LHM, the phase velocity is in the opposite direction of the energy flow in the sense that the energy flow leaves the source in waves with a phase velocity pointing backward.

- Veselago also predicted that the **Doppler and Cerenkov effects** will be reversed in LHM. An approaching source will appear to radiate at a lower frequency and charged particles moving faster than the speed of light in the medium will radiate in a backward cone, not a forward cone. These two exotic properties are not employed in this thesis, however details about them can be found in [3].

3.4 Applications of LHMs

LHMs with a negative refractive index would enable some new devices to be created. At optical and microwave frequencies, it could be possible to build a complete planar lens that nevertheless focuses light to a perfect geometric point [10]. Instead of grinding the lens to specific convex or concave angles, LHMs combined with traditional materials

should be able to serve all lens needs with easy-to-make planar surfaces. A lightweight concave lens made from LHMs could do the same job as a convex lens made from conventional material, which is much heavier, more expensive and more difficult to manufacture. One application, under development by Boeing Company in United States, is to uses lenses made of LHMs for radar.

As outlined in the last section, the wave in LHMs propagates in the backward direction. Thus, LHMs can be employed to design a phase shifter, which exhibits a linear phase response with frequency [11]. Especially, the phase of the wave can be kept unchanged after the wave passes through one vacuum slab and one LHM slab that have the same thickness and absolute value of refractive index but opposite sign. This property may be applied to construct zero phase delay transmission line to feed antenna arrays.

Usually, a normal lens cannot produce an image better resolved than one wavelength, since the evanescent wave containing the finest details of an object is confined to the vicinity of the source and cannot be restored by the normal lens. However, an evanescent wave entering LHM is actually amplified due to the excitation surface Plasmon resonance at the RHM/LHM interface [12]. Thus the one-wavelength resolution limitation can be broken and LHM lens could focus light into an area smaller than its wavelength creating sharper beams that could, for example, be used to burn more information onto CDs and DVDs or etch more tightly packed features onto semiconductor chips [13]. Now, the amount of information that can be written onto a CD or DVD is limited by the diameter of a laser beam, which is limited by the wavelength of

laser light. One feature film can be comfortably recorded onto one DVD at present. If the laser light can be focused to a spot much smaller than its wavelength, up to 1,000 movies can be recorded on each DVD.

3.5 Numerical Techniques for LHMs

In order to verify the predicted properties of LHMs and simulate electromagnetic wave interaction with LHMs, the importance of full-wave numerical simulations is enormous as available experimental data is very limited. So far, several numerical methods have been employed to investigate the properties of LHMs. In [14], the Transfer Matrix Method (TMM) is employed to calculate the transmission, reflection and phase properties of LHMs. However, the method of TMM cannot describe the time evolution of the electromagnetic field interaction with LHMs. The dispersive FDTD method, one of the best available full-wave numerical methods, has been proved to be able to investigate the properties of LHMs successfully and thus will be employed in this thesis.

Some commercial software's have been employed to investigate the properties of LHMs as well. High Frequency Structure Simulator (HFSS), a commercial finite-element based electromagnetic solver, has been employed to study the electromagnetic scattering properties of LHMs [15]. In [16], Microwave studio (MWS), which is based on the finite integration technique, has been used to calculate the transmission properties of LHMs.

Why choose the dispersive FDTD method in this thesis? Firstly, in FDTD, the results are directly obtained from Maxwell's equations and the constitutive relations of

the materials, so that unnecessary assumptions and unessential complications can be avoided. Secondly, the FDTD method is a time-domain method, thus it can provide detailed and accurate description on the temporal dynamics of the interaction between electromagnetic waves and LHMs. Thirdly, FDTD can simulate the evanescent mode wave interaction with LHM structures. This is very important because some applications on LHMs are dependent on evanescent waves and thus a method that models evanescent waves in EM structures comprising of LHM components is essential. Fourthly, FDTD is a powerful tool that could be applied to antenna problems [17], for example, it can predict antenna patterns and terminal impedances in a straightforward manner. Therefore the FDTD method is a good tool that can be employed to design antennas related to LHMs. It is also very easy to implement using any of the available programming languages such as Fortran or MATLAB.

3.5.1 Characterization of LHMs

Since the dispersive FDTD method will be employed to investigate LHMs in this thesis, the details on how to characterize LHMs with a dispersive FDTD method will be presented in this section. As outlined above, LHMs have simultaneous negative permittivity and permeability; it is worth noting that simultaneous negative values of permittivity and permeability can be realized only when there is frequency dispersion. This can be seen from the relation between energy density W and electric field E and magnetic field H.

$$W = \frac{1}{2}\varepsilon E^2 + \frac{1}{2}\mu H^2 \qquad (3.5.1.1)$$

If both ε and μ are negative values and they are non-dispersive, the total energy would be negative in this case, that will break the normal law of energy. When there is frequency dispersion, the relation (3.5.1.1) will be replaced as in [9] by,

$$W = \frac{1}{2}\left\{\frac{\partial\left[\varepsilon(\omega)\omega\right]}{\partial\omega}E^2 + \frac{\partial\left[\mu(\omega)\omega\right]}{\partial\omega}H^2\right\} \tag{3.5.1.2}$$

For the energy density given by equation (3.5.1.2) to be positive, it is required that $\varepsilon(\omega)$ and $\mu(\omega)$ must satisfy the following constraints.

$$\frac{\partial\left[\varepsilon(\omega)\omega\right]}{\partial\omega} > 0 \tag{3.5.1.3a}$$

$$\frac{\partial\left[\mu(\omega)\omega\right]}{\partial\omega} > 0 \tag{3.5.1.3b}$$

As suggested in [18], realistic LHMs can be characterized by the Drude mode [19] as:

$$\varepsilon_r(\omega) = 1 - \frac{\omega_{ep}^2}{\omega^2 - j\omega\tau_e} \tag{3.5.1.4a}$$

$$\mu_r(\omega) = 1 - \frac{\omega_{em}^2}{\omega^2 - j\omega\tau_m} \tag{3.5.1.4b}$$

ω_{ep} is the electric plasma frequency and τ_e is the electric damping factor related to loss. Likewise, ω_{mp} is the magnetic plasma frequency and τ_m is the magnetic damping factor related to loss. It can be shown that the permittivity function (3.5.1.4a) and the permeability function (3.5.1.4b) satisfy the constraints of (3.5.1.3a) and (3.5.1.3b) respectively and thus they will be employed to characterize LHMs in this thesis.

3.5.2 Available FDTD Techniques for LHM Modeling

FDTD was proposed with the assumption that medium was non-dispersive. To model dispersive medium, the standard Yee time-stepping equations need to be modified. Several techniques have been proposed to incorporate frequency dispersion into the FDTD models. They can roughly be categorized into three types: Recursive Convolution (RC) method [20], Auxiliary Differential Equation (ADE) method [21] and Z-transform (ZT) method [22].

In summary, the RC method discussed here is first-order accurate in time while the original ADE approach is temporally second-order accurate. The disadvantage of the original ADE method is that it is memory intensive. However, the LHMs in this thesis are characterized by Drude medium models, thus the required additional storage for the original ADE approach is not significant. Taking account of the need for the Uniaxial Perfect Matched Layer (UPML) [23] Absorbing Boundary Condition (ABC) for dispersive medium, which will be briefly discussed in this chapter, the original ADE approach is the one being implemented easily and requiring minimal numerical coding effect. Consequently, the original ADE approach is chosen here to model LHMs.

3.6 ADE FDTD for LHM Modeling

The ADE approach is a two step approach. The constitutive relations are employed to find the corresponding electric or magnetic field components. The frequency domain equations are transformed to time domain using Inverse Fourier Transforms. A Second order central difference scheme is then applied to discretize the arithmetic operators. A

semi-implicit scheme is to be used in order to get rid of instability in the code. The fields F^n at time $t = n\Delta t$ are approximated by,

$$F^n = \frac{F^{n+1} + 2F^n + F^{n-1}}{4} \tag{3.6.1}$$

Consider a 2D TE case consisting of field components $E_z, H_x \; and \; H_y$. The 2D FDTD simulator involves the following set of equations,

$$\frac{\partial D_z}{\partial t} = \frac{\partial H_y}{\partial x} - \frac{\partial H_x}{\partial y} \tag{3.6.2a}$$

$$D_z = \varepsilon_0 (1 - \frac{\omega_{ep}^2}{\omega^2 - j\omega\tau_e}) E_z \tag{3.6.2b}$$

$$\frac{\partial B_x}{\partial t} = -\frac{\partial E_z}{\partial y} \tag{3.6.2c}$$

$$B_x = \mu_0 (1 - \frac{\omega_{em}^2}{\omega^2 - j\omega\tau m}) H_x \tag{3.6.2d}$$

$$\frac{\partial B_y}{\partial t} = \frac{\partial E_z}{\partial x} \tag{3.6.2e}$$

$$B_y = \mu_0 (1 - \frac{\omega_{em}^2}{\omega^2 - j\omega\tau m}) H_y \tag{3.6.2f}$$

Since multiplication by $j\omega$ in the frequency domain are equivalent to time derivatives in time domain, equations (3.6.2b), (3.6.2d) and (3.6.2f) are equivalent to

$$\frac{\partial^2 D_z}{\partial t^2} + \tau_e \frac{\partial D_z}{\partial t} = \varepsilon_0 \frac{\partial^2 E_z}{\partial t^2} + \varepsilon_0 \tau_e \frac{\partial E_z}{\partial t} + \varepsilon_0 \omega_{ep}^2 E_z \tag{3.6.3a}$$

$$\frac{\partial^2 B_x}{\partial t^2} + \tau_m \frac{\partial B_x}{\partial t} = \mu_0 \frac{\partial^2 H_x}{\partial t^2} + \mu_0 \tau_m \frac{\partial H_x}{\partial t} + \varepsilon_0 \omega_{ep}^2 H_x \tag{3.6.3b}$$

$$\frac{\partial^2 B_y}{\partial t^2}+\tau_m\frac{\partial B_y}{\partial t}=\mu_0\frac{\partial^2 H_y}{\partial t^2}+\mu_0\tau_m\frac{\partial H_y}{\partial t}+\varepsilon_0\omega_{mp}^2 H_y \tag{3.6.3c}$$

Applying second order FDTD discretization both in space and time to equations (3.6.2a), (3.6.2c) and (3.6.2e),

$$D_z^{n+1}(i+1/2,j+1/2)=D_z^{n}(i+1/2,j+1/2)+\Delta t\left[\frac{H_y^{n+1/2}(i+1,j+1/2)-H_y^{n+1/2}(i,j+1/2)}{\Delta x}-\frac{H_x^{n+1/2}(i+1,j+1/2)-H_x^{n+1/2}(i,j+1/2)}{\Delta y}\right] \tag{3.6.4a}$$

$$B_x^{n+3/2}(i+1/2,j+1)=B_x^{n+1/2}(i+1/2,j+1)-\Delta t\left[\frac{E_z^{n+1}(i+1/2,j+3/2)-E_z^{n+1}(i+1/2,j+1/2)}{\Delta y}\right] \tag{3.6.4b}$$

$$B_y^{n+3/2}(i+1,j+1/2)=B_y^{n+1/2}(i+1,j+1/2)+\Delta t\left[\frac{E_z^{n+1}(i+3/2,j+1/2)-E_z^{n+1}(i+1/2,j+1/2)}{\Delta x}\right] \tag{3.6.4c}$$

Applying the semi-implicit scheme along with second order FDTD discretization both in space and time to equation (3.6.3a), the explicit time-stepping expression for E_z is derived as follows,

$$E_z^{n+1}(i+1/2,j+1/2)=\sum_{i=-1}^{1}a_i D_z^{n+i}(i+1/2,j+1/2)-\sum_{i=-1}^{0}b_i E_z^{n+i}(i+1/2,j+1/2) \tag{3.6.5}$$

where

$$a_1=\frac{4+2\tau_e\Delta t}{A_1} \tag{3.6.6a}$$

$$a_0=\frac{-8}{A_1} \tag{3.6.6b}$$

$$a_{-1}=\frac{4-2\tau_e\Delta t}{A_1} \tag{3.6.6c}$$

$$b_0 = \frac{-8\varepsilon_0 + 2\varepsilon_0 \Delta t^2 \omega_{ep}^2}{A_1} \tag{3.6.6d}$$

$$b_{-1} = \frac{4\varepsilon_0 - 2\varepsilon_0 \tau_e \Delta t + \varepsilon_0 \Delta t^2 \omega_{ep}^2}{A_1} \tag{3.6.6e}$$

$$A_1 = 4\varepsilon_0 + 2\varepsilon_0 \tau_e \Delta t + \varepsilon_0 \Delta t^2 \omega_{ep}^2 \tag{3.6.6f}$$

The same approach can be applied to equations (3.6.3b) and (3.6.3c) to yield H_x and H_y respectively.

$$H_x^{n+3/2}(i+1/2, j+1) = \sum_{i=-1}^{1} c_i B_x^{n+i+1/2}(i+1/2, j+1) - \sum_{i=-1}^{0} d_i B_x^{n+i+1/2}(i+1/2, j+1) \tag{3.6.7a}$$

$$H_y^{n+3/2}(i+1, j+1/2) = \sum_{i=-1}^{1} c_i B_y^{n+i+1/2}(i+1, j+1/2) - \sum_{i=-1}^{0} d_i B_y^{n+i+1/2}(i+1, j+1/2) \tag{3.6.7b}$$

where

$$c_1 = \frac{4 + 2\tau_m \Delta t}{A_2} \tag{3.6.8a}$$

$$a_0 = \frac{-8}{A_2} \tag{3.6.8b}$$

$$a_{-1} = \frac{4 - 2\tau_m \Delta t}{A_2} \tag{3.6.8c}$$

$$d_0 = \frac{-8\mu_0 + 2\mu_0 \Delta t^2 \omega_{mp}^2}{A_2} \tag{3.6.8d}$$

$$d_{-1} = \frac{4\mu_0 - 2\mu_0 \tau_m \Delta t + \mu_0 \Delta t^2 \omega_{mp}^2}{A_2} \tag{3.6.8e}$$

$$A_2 = 4\mu_0 + 2\mu_0 \tau_m \Delta t + \mu_0 \Delta t^2 \omega_{mp}^2 \tag{3.6.8f}$$

Thus, the iteration procedure of ADE FDTD on LHMs can be summarized in Figure 3.2.

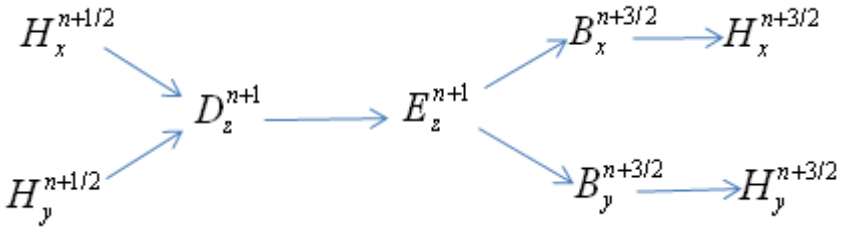

Figure 3.2: *Iteration Procedure of ADE FDTD for LHMs*

3.7 Validating the FDTD Code

To validate both the ADE FDTD code, a test scheme is shown in Figure 3.2(a)-(d). The simulation proves the inverse Snell's law for the metamaterials. A sinusoidal continuous wave point source of frequency 5 GHz is used to excite the 320 by 320 grid. In order to truncate the computational grid, an absorbing boundary condition called the Uniaxial perfectly matched layer (UPML) [18] is used. The UPML boundary of order 4 extends 15 cells in each direction. The spatial increments are chosen to be $1/40^{th}$ of the incident wavelength and the time increment has been decided by the courant condition. The source is placed 40 cells away from the metamaterial slab. The slab is 80 cells wide. As seen in figure 3.2(d), the original source reappears in the metamaterial slab as well as in the region after the slab.

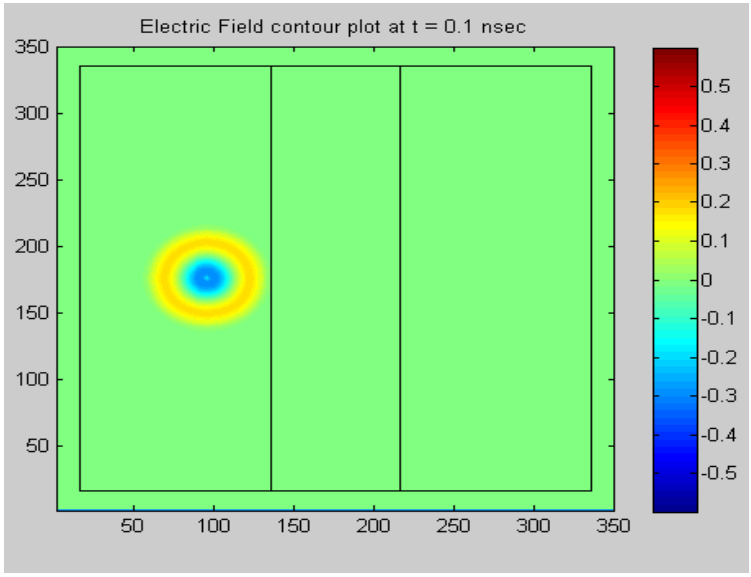

Figure 3.3(a): *FDTD Simulation of Gaussian source adjacent to a metamaterial slab at time t = 0.1 nsec.*

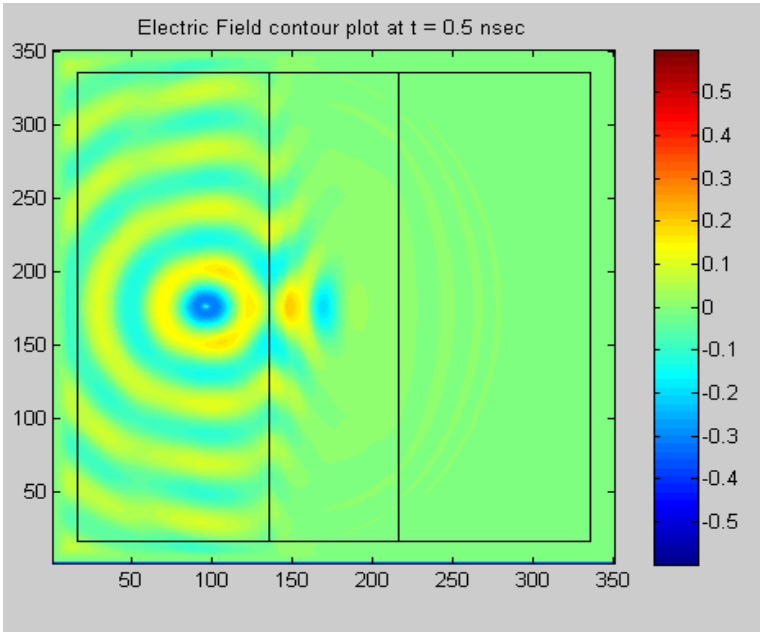

Figure 3.3(b): *FDTD Simulation of Gaussian source adjacent to a metamaterial slab at time t = 0.5 nsec.*

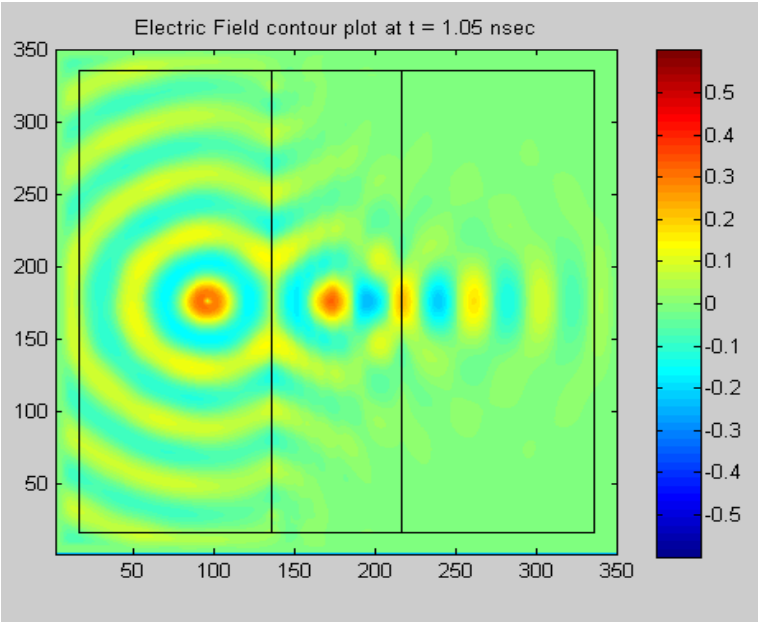

Figure 3.3(c): *FDTD Simulation of Gaussian source adjacent to a metamaterial slab at time t = 10.5 nsec.*

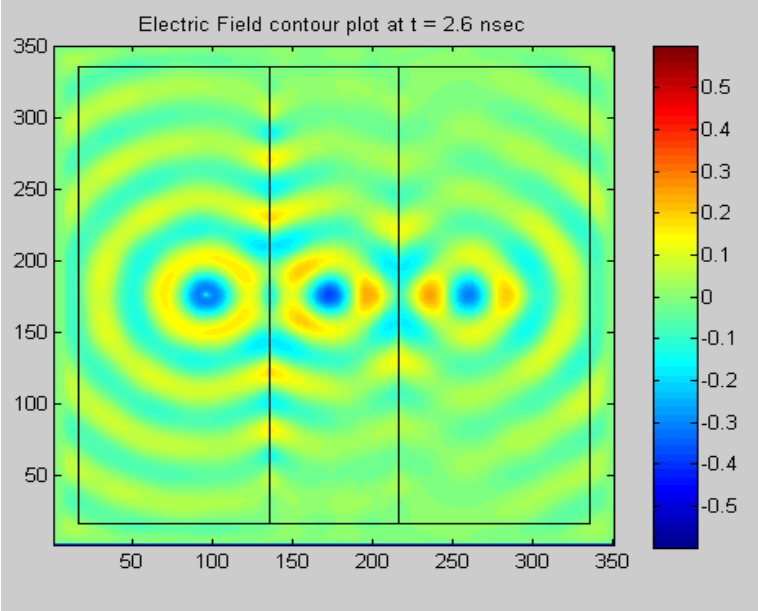

Figure 3.3(d): *FDTD Simulation of Gaussian source adjacent to a metamaterial slab at time t = 2.6 nsec.*

3.8 Summary

In this chapter, properties of metamaterials have been briefly discussed. FDTD implementation of metamaterials along with UPML boundary conditions have also been touched upon. To validate the code, a test scheme designed to show the Inverse Snall's law for metamaterials.

CHAPTER IV

ELECTRICALLY SMALL ANTENNAS

4.1 Introduction

Antennas which are small, efficient and have significant bandwidth would fulfill many of today's emerging wireless technology requirements, especially in the areas of communication and sensor networks. Such devices also called as Electrically Small Antennas (ESAs), have some contradictory demands to be met in order to be a good radiator. There are physical limitations on antenna performance related to the size of the antenna and the limits are difficult to reach.

This chapter introduces various properties of ESAs along with a brief discussion of their characteristics. A modified form of Catheter antenna in [1] which falls under the category of an ESA will be modeled using FDTD technique. The Catheter antenna design is discussed in a step by step manner and at each step FDTD is used to analyze the antenna. The final Catheter antenna results obtained using FDTD is matched to the measured results in [24].

4.2 Electrically Small Antennas

Wheeler [25] in 1947 was the first one to look at the fundamental limitations of ESAs. He defined ESA as one whose maximum dimension is less than $\frac{\lambda}{2\pi}$. In other words an antenna where,

$$ka < 1 \tag{4.2.1}$$

$k = \frac{2\pi}{\lambda}$ (radians/meter) is the propagation constant

λ (meter) is the free space wavelength at resonance

a is the radius of sphere enclosing the maximum dimensions of the antenna

This is illustrated in figure 4.1.

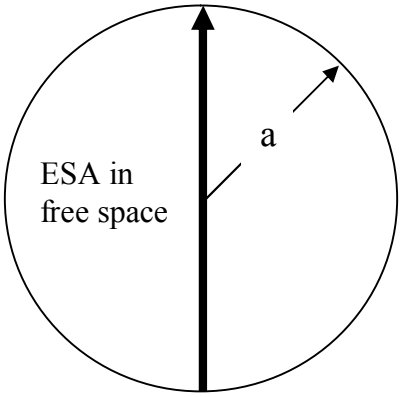

Figure 4.1: *Sphere enclosing an electrically small radiating element*

L. J. Chu [26] in 1948 determined he fundamental limits on the radiation quality factor Q, associated with ESAs in what is now called as Chu's limit. The quality factor of an antenna is defined as,

$$Q = \frac{2\pi(Peak\ energy\ stored)}{Power\ lost\ per\ period} \tag{4.2.2}$$

The Quality factor or Q factor characterizes the bandwidth of a resonator relative to the center frequency. If f_{+3dB} and f_{-3dB} represent the 3 dB cutoff frequencies above and below the resonant frequency, the fractional bandwidth (FBW) is related to Q factor as,

$$Q = \frac{1}{FBW} \tag{4.2.3}$$

where

$$FBW = \frac{\Delta f_{3dB}}{f_0} \tag{4.2.4}$$

f_0 is the center frequency and,

$$\Delta f_{3dB} = f_{+3dB} - f_{-3dB}$$

Therefore,

$$Q = \frac{f_0}{\Delta f_{3dB}} \tag{4.2.6}$$

Higher Q values lead to lower FBW or narrowband and lower Q values lead to higher FBW or broadband. Chu's limit is the minimum Q value attainable by an ESA has been shown to be,

$$Q_{chu} = \frac{1 + 2(ka)^2}{(ka)^3\left[1 + (ka)^2\right]} \tag{4.2.7}$$

A more exact result for the limits on Q factor was shown by McLean [27], although still referred to as Chu limit is,

$$Q_{chu} = \frac{1}{(ka)} + \frac{1}{(ka)^3} \tag{4.2.8}$$

If $ka << 1$, the Chu limit reduces to,

$$Q_{chu} = \frac{1}{(ka)^3} \tag{4.2.9}$$

These equations are valid for a perfect lossless matching network. Figure 4.2 shows the difference between the approximated Chu's limit and the original Chu limit.

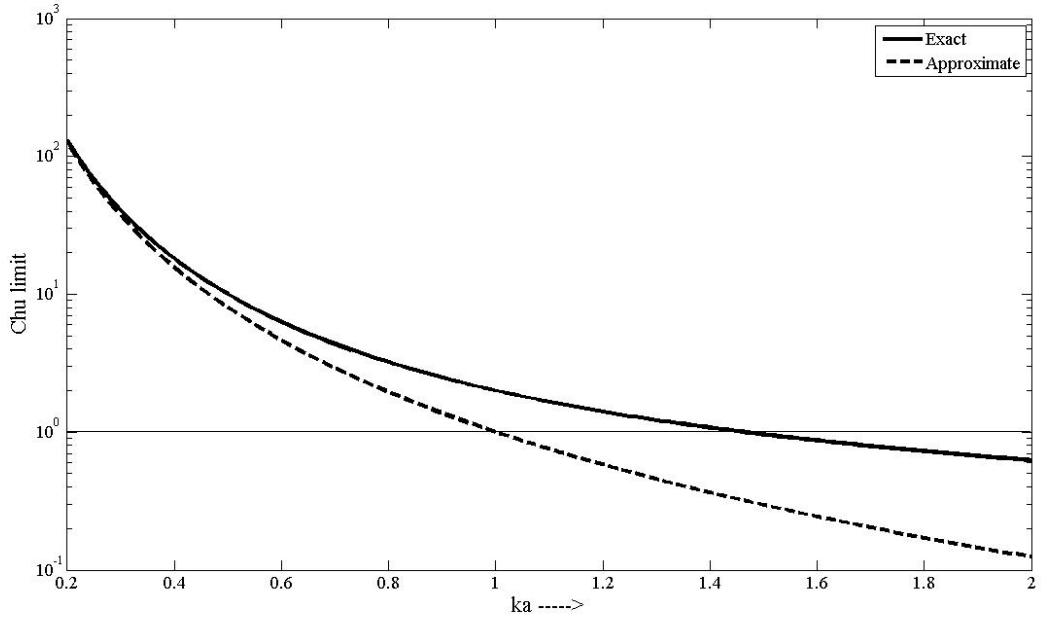

Figure 4.2: *Q vs. ka for exact and approximated Chu limit*

We observe from the plot that for small values of ka (0.2-0.5), the difference between the approximated and exact Chu limit is negligible for all practical purposes. As the size of the antenna decreases, the Chu limit or the minimum Q value attainable dramatically

increases. This causes a decrease in the maximum fractional bandwidth attainable by an ESA. The Q factor and FBW will approach the Chu limit only if one efficiently utilizes the available volume in designing the ESA.

4.3 Microwave Catheter Antenna

Transcatheter ablation is a non surgical procedure for localized destruction of cardiac tissue involved in generating disturbances of cardiac rhythm. One of the many methods available for transcatheter ablation involves the use of Catheter Antenna, a microwave antenna system [24]. Because of the operating environment, the Catheter antenna has to be extremely small in size. Figure 4.4 shows a catheter antenna described in [24] which will be used modified to include a metamaterial coating in later part of the thesis.

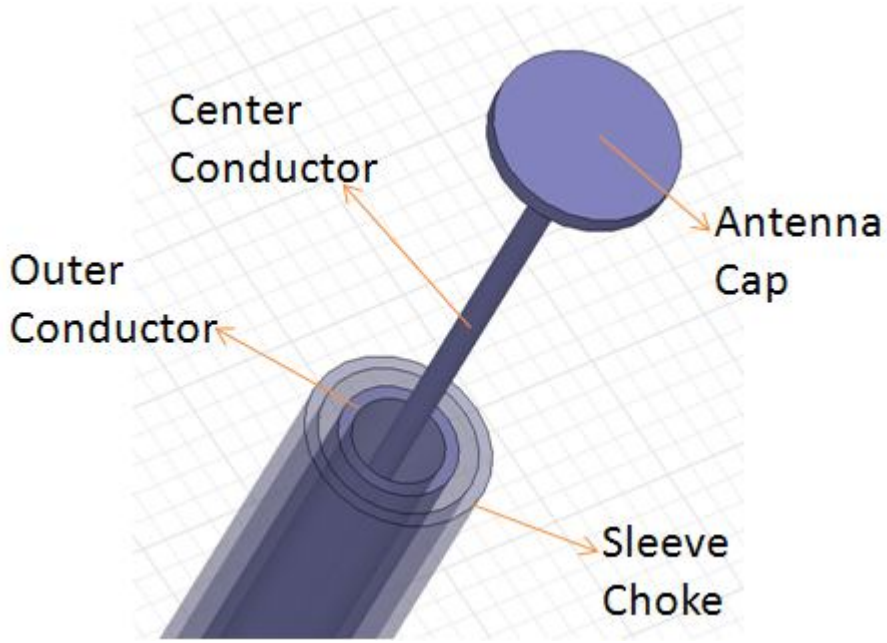

Figure 4.3: (a) *3D view of the catheter antenna without Teflon coating*

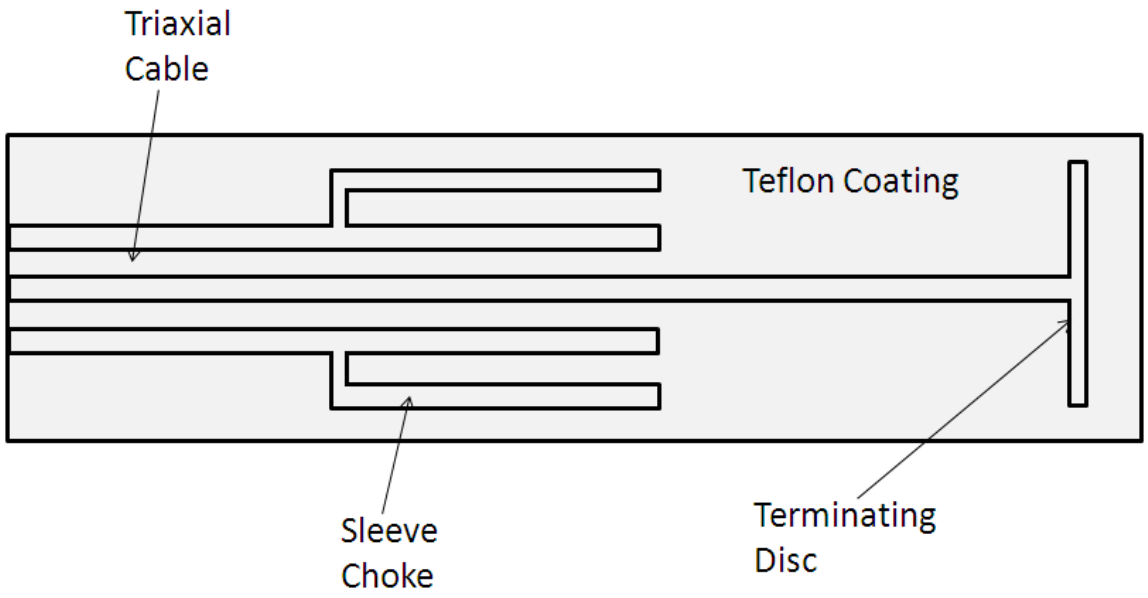

Figure 4.3: (b) *Cross sectional view of the catheter antenna*

The Catheter Antenna is rotationally symmetric. This aspect of the antenna will be exploited while numerically modeling the antenna using FDTD. Further the symmetry in figure 4.3(b) will be used to reduce the computational burden for faster analysis. Figure 4.4shows the dimensions of the Catheter Antenna.

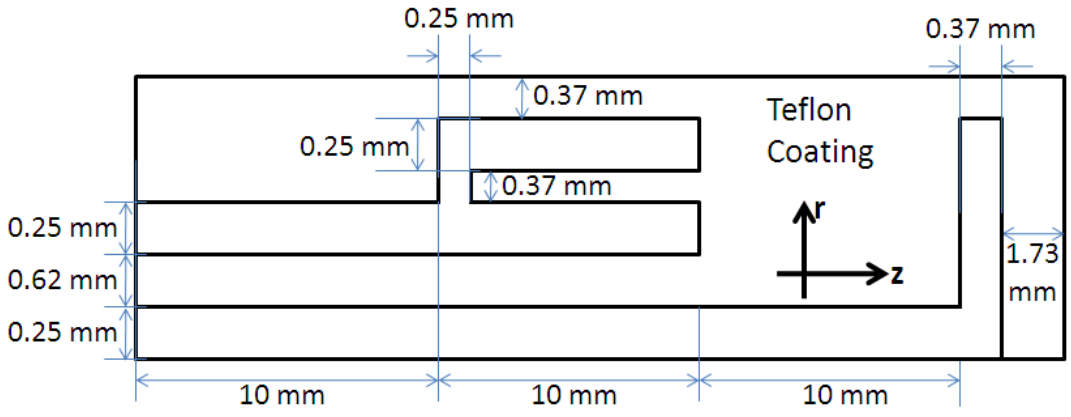

Figure 4.4: *Cross sectional view of the catheter antenna with dimensions*

4.4 FDTD Formulation of the Antenna Problem

The antenna considered in figure 4.4 is symmetric in cylindrical coordinates and is exited by a rotationally symmetric source. Therefore the electromagnetic field is independent of the cylindrical coordinate ϕ. Maxwell equations can be uncoupled into two independent sets: one that involves the components E_φ, H_r, H_z, the TE field; one that involves the components H_φ, E_r, E_z, the TM field. Since the excitation for the antenna is Transverse Electromagnetic Mode (TEM) which has only H_φ, E_r, only the rotationally symmetric TM modes are excited [28]. The relevant Maxwell's equations in time domain are given by,

$$\frac{1}{r}\frac{\partial(rH_\varphi)}{\partial r} = \varepsilon_0\varepsilon_r\frac{\partial(E_z)}{\partial t} + \sigma E_z \tag{4.4.1a}$$

$$-\frac{\partial(rH_\varphi)}{\partial z} = \varepsilon_0\varepsilon_r\frac{\partial(E_r)}{\partial t} + \sigma E_r \tag{4.4.1b}$$

$$\frac{\partial(E_r)}{\partial z} - \frac{\partial(E_z)}{\partial r} = -\mu_0\mu_r\frac{\partial(H_\varphi)}{\partial t} \tag{4.4.1c}$$

Equations (4.4.1a), (4.4.1b) and (4.4.1c) are discretized in space and time using the Yee's FDTD methods as in Chapter II of the thesis. The Maxwell's equations after discretized are,

$$E_z^{n+1}(i,j) = E_z^n(i,j)\frac{(2\varepsilon_o\varepsilon_r - \sigma\Delta t)}{(2\varepsilon_o\varepsilon_r + \sigma\Delta t)} + \frac{2\Delta t}{(2\varepsilon_o\varepsilon_r + \sigma\Delta t)}\left\{r_j H_\phi(i,j) - r_{j-1}H_\phi(i,j-1)\right\} \tag{4.4.2a}$$

$$E_r^{n+1}(i,j) = E_r^n(i,j)\frac{(2\varepsilon_o\varepsilon_r - \sigma\Delta t)}{(2\varepsilon_o\varepsilon_r + \sigma\Delta t)} + \frac{2\Delta t}{(2\varepsilon_o\varepsilon_r + \sigma\Delta t)}\left\{r_j H_\phi(i,j) - r_{j-1}H_\phi(i-1,j)\right\} \tag{4.4.2b}$$

$$H_{\phi}^{n+1}(i,j) = H_{\phi}^{n}(i,j) + \frac{\Delta t}{2\mu_o\mu_r\Delta r}\{E_z(i,j+1) - E_z(i,j)\} - \frac{\Delta t}{2\mu_o\mu_r\Delta r}\{E_r(i+1,j) - E_z(i,j)\} \quad (4.4.2c)$$

The incident electric field is given by,

$$\vec{E}_{source} = \frac{g(t)}{\ln(b/a)r}\hat{r} \quad (4.4.3)$$

where g(t) is the Gaussian source and a, b are the inner and outer radii of the coax feed. Since we plan to model only half of the antenna structure as shown in figure 4.4, at the boundary r = 0, we need to implement the symmetric condition.

$$\lim_{r\to 0}\left(\frac{1}{r}\frac{\partial(rH_{\varphi})}{\partial r}\right) = \lim_{r\to 0}\left(\frac{\frac{\partial(rH_{\varphi})}{\partial r}}{r}\right) \quad (4.4.4)$$

As $r \to 0$, both the denominator and the numerator tend to zero. Using L'Hospitals rule,

$$\lim_{r\to 0}\left(\frac{\frac{\partial(rH_{\varphi})}{\partial r}}{r}\right) = \lim_{r\to 0}\left(\frac{\frac{\partial^2(rH_{\varphi})}{\partial^2 r}}{\frac{\partial(r)}{\partial r}}\right)$$

$$= \lim_{r\to 0}\left(\frac{\partial H_{\varphi}}{\partial r} + \frac{\partial H_{\varphi}}{\partial r} + r\frac{\partial^2 H_{\varphi}}{\partial^2 r}\right) \quad (4.4.5)$$

$$= 2\frac{\partial H_{\varphi}}{\partial r} \qquad at\ r = 0$$

At r = 0, H_{φ} curls around E_z . Hence equation (4.4.5) can be written as,

$$2\frac{\partial H_{\varphi}}{\partial r} = \frac{2H_{\varphi}(i,1)}{\Delta r} \quad (4.4.6)$$

To calculate the field components on the rest of the boundary, Circular Liao boundary condition [29] is used. The Courant-Friedrichs condition for stability is given by,

$$c\Delta t \leq \sqrt{\frac{\Delta r^2 \Delta z^2}{\Delta r^2 + \Delta z^2}} \tag{4.4.7}$$

4.5 FDTD Simulation of the Catheter Antenna

To validate the FDTD code, the antenna in [24] is simulated starting from a monopole to the one in figure 4.4. The antenna is given a Teflon coating to prevent it from coming in contact with human tissue. The Teflon has a permittivity of 2.03. The antenna is placed in blood medium with permittivity of 50.3 and a conductivity of 2.0145. The space increments $\Delta r, \Delta z$ are set to 0.123 mm in order to have at least 5 cells in the coax cable where the source excitation is placed.

4.5.1 Monopole Antenna

Figure 4.5(a) shows the monopole antenna along with its dimensions. Figure 4.5(b) shows the S11 parameters of the antenna. Figure 4.5(c) shows the Specific absorption rate (SAR) profile of antenna.

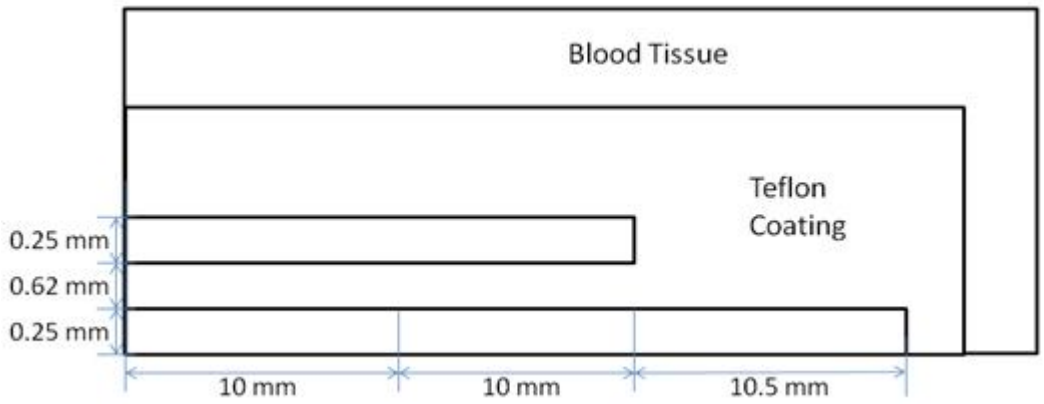

Figure 4.5(a): *Monopole Antenna in blood medium along with dimensions*

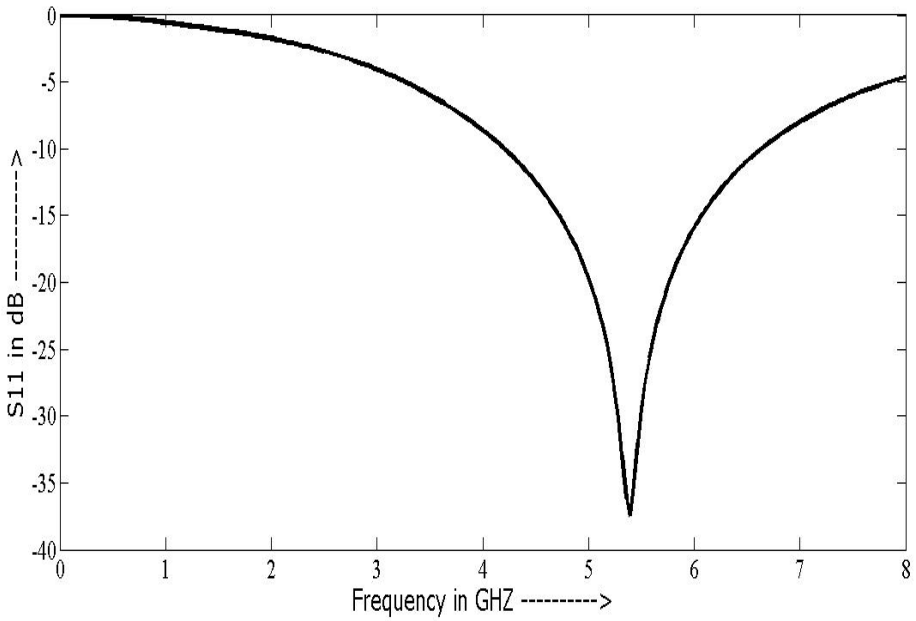

Figure 4.5(b): *S11 for the Monopole Antenna in blood medium*

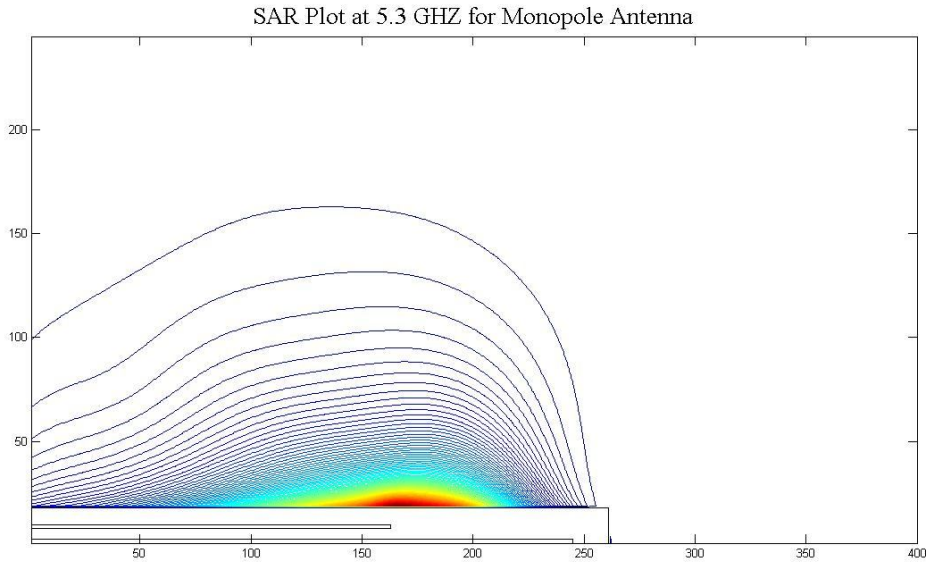

Figure 4.5(c): *SAR profile* for the *Monopole Antenna in blood medium*

The SAR gives a measure of amount of RF energy absorbed by a lossy medium. It is given by,

$$SAR = \frac{\sigma E^2}{\rho} \tag{4.5.1.1}$$

The monopole with a length of 10.37 mm immersed in Teflon medium should resonate at 5.05 GHz. The resonant frequency of the antenna by FDTD simulation is found to be 5.39 GHz. The slight shift in the resonant frequency can be attributed to the lossy blood medium around the antenna and the discretization of the antenna. The 10 dB bandwidth has been found to be 2.454 GHz. The FDTD results match with the published results in [24].

4.5.2 Monopole Antenna with Terminating Cap

Figure 4.6(a) shows the monopole antenna along with its dimensions. Figure 4.6(b) shows the S11 parameters of the antenna. Figure 4.6(c) shows the Specific absorption rate profile of antenna.

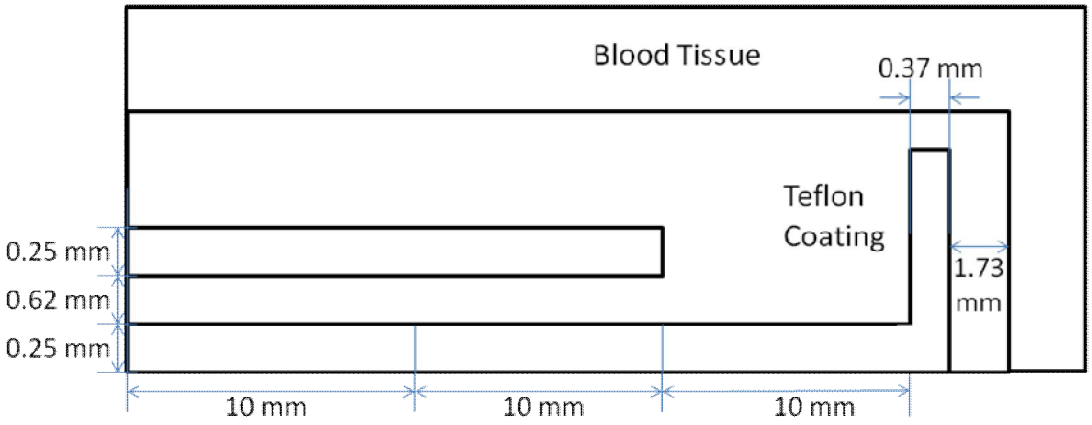

Figure 4.6(a): *Antenna with termination cap in blood medium along with dimensions*

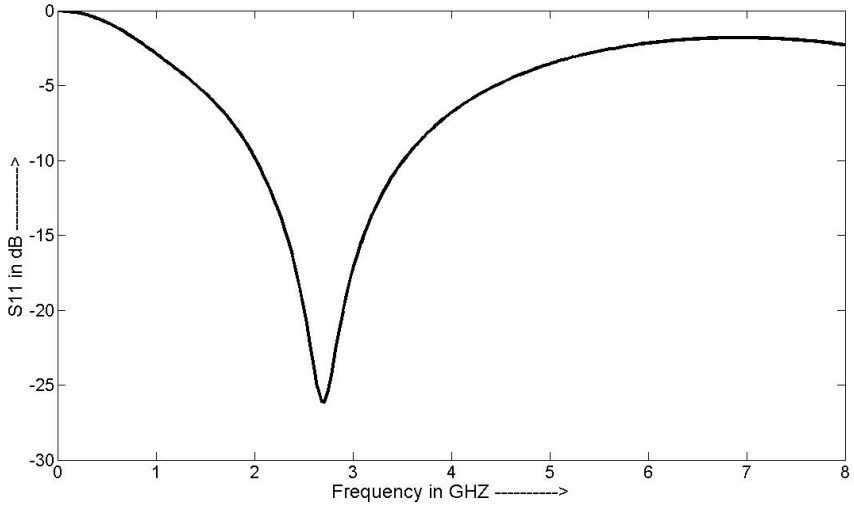

Figure 4.6(b): *S11 for the antenna with termination cap in blood medium*

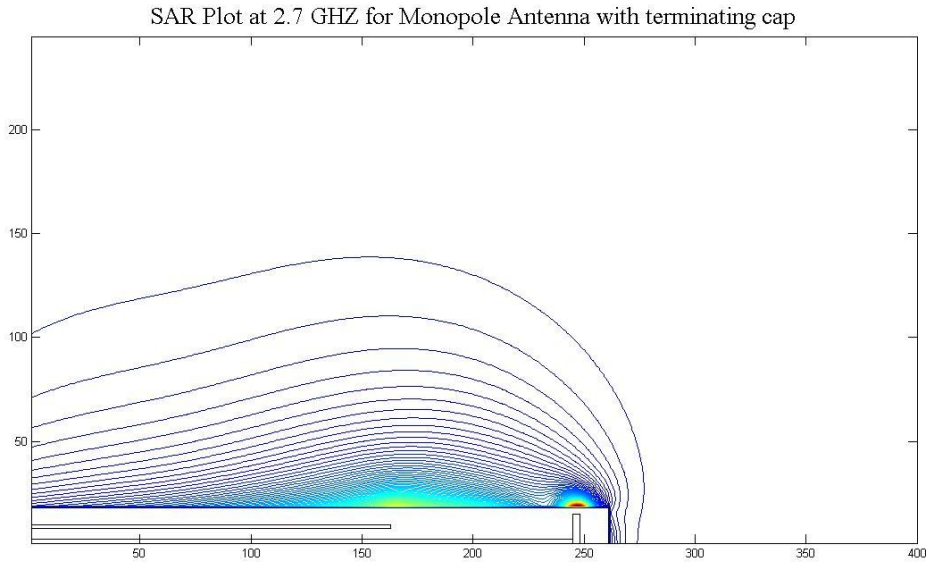

Figure 4.6(c): *SAR profile for the antenna with termination cap in blood medium*

The monopole with a termination cap resonates at 2.71 GHz. The 10 dB bandwidth has been found to be 1.462 GHz. The FDTD results match with the published results in [24]. From the SAR profile it is evident that there is a lot of power dissipation towards the back end of the antenna. To get rid of this, a sleeve choke is used.

4.5.3 Monopole Antenna with Terminating Cap and Choke

Figure 4.7(a) shows the monopole antenna along with the terminating cap and the choke. Figure 4.7(b) shows the S11 parameters of the antenna. Figure 4.7(c) shows the Specific absorption rate profile of antenna.

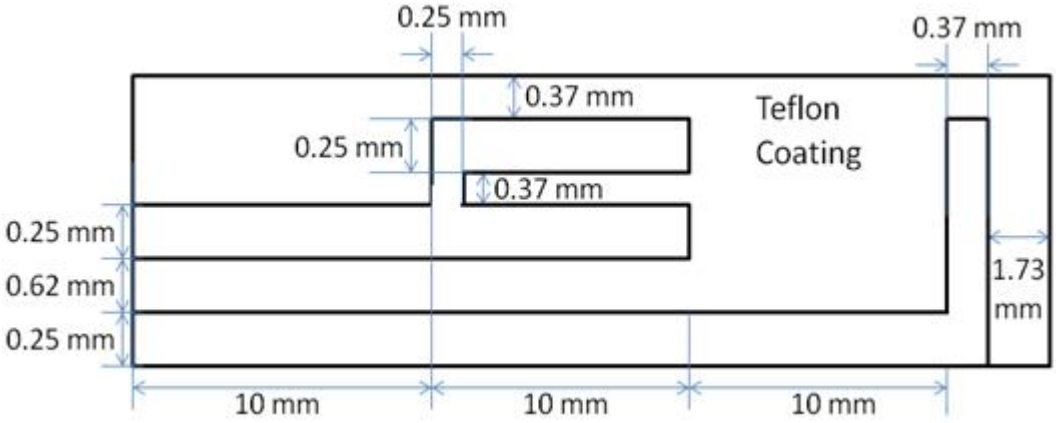

Figure 4.7(a): *Antenna with termination cap and Sleeve choke in blood medium along with dimensions*

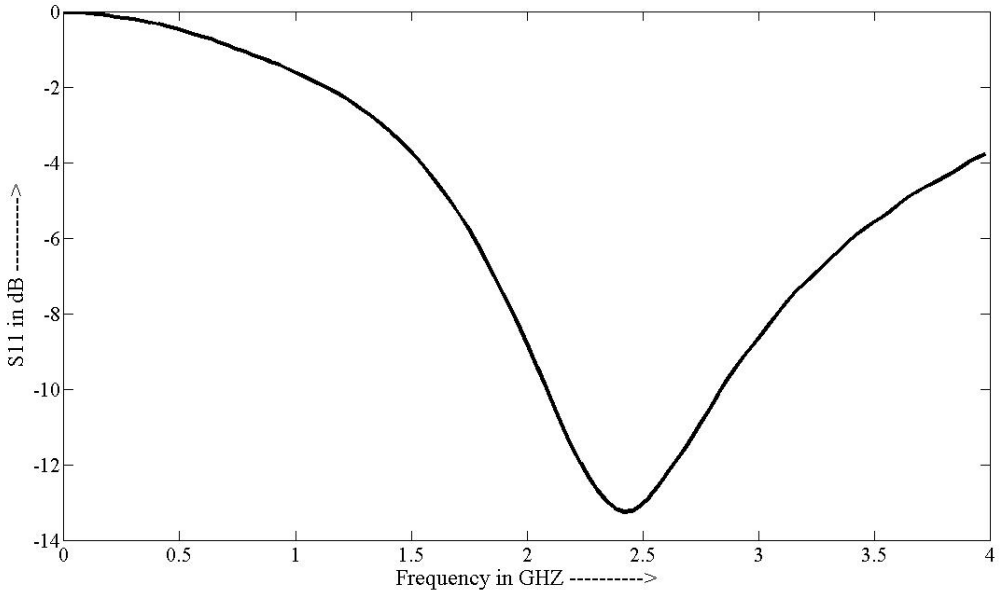

Figure 4.7(b): *S11 for antenna the with termination cap and Sleeve choke in blood medium*

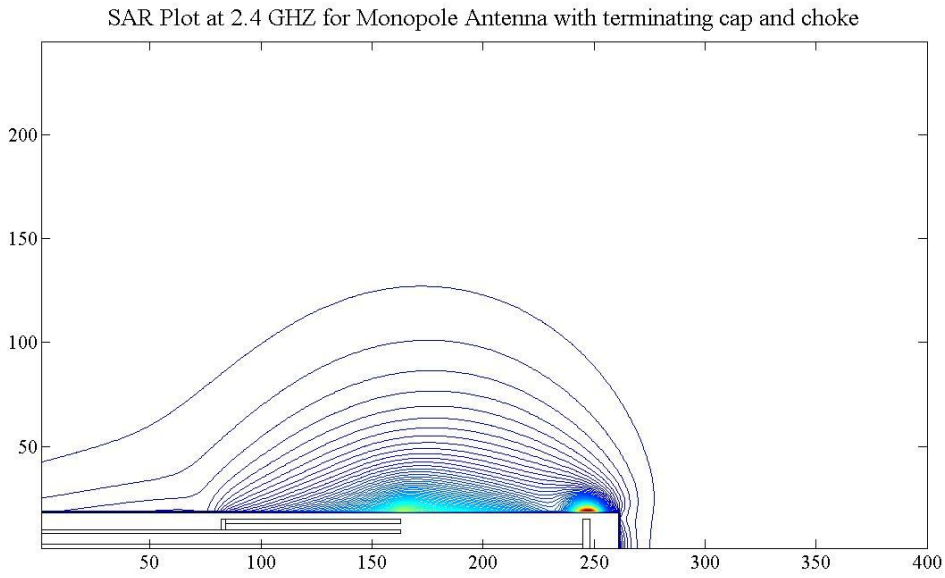

Figure 4.7(c): *SAR profile for the antenna with termination cap and Sleeve choke in blood medium*

The monopole with termination cap and sleeve choke resonates at 2.41 GHz. The 10 dB bandwidth has been found to be 0.82 GHz. The FDTD results match with the published results in [24]. From the SAR profile, it is evident that the power dissipation is towards the front of the antenna.

4.5.4 Monopole Antenna with Terminating Cap, Choke and Dielectric

Figure 4.8(a) shows the monopole antenna along with the terminating cap, the choke and a dielectric with a permittivity of 12. Figure 4.8(b) shows the S11 parameters of the antenna. Figure 4.8(c) shows the Specific absorption rate profile of antenna.

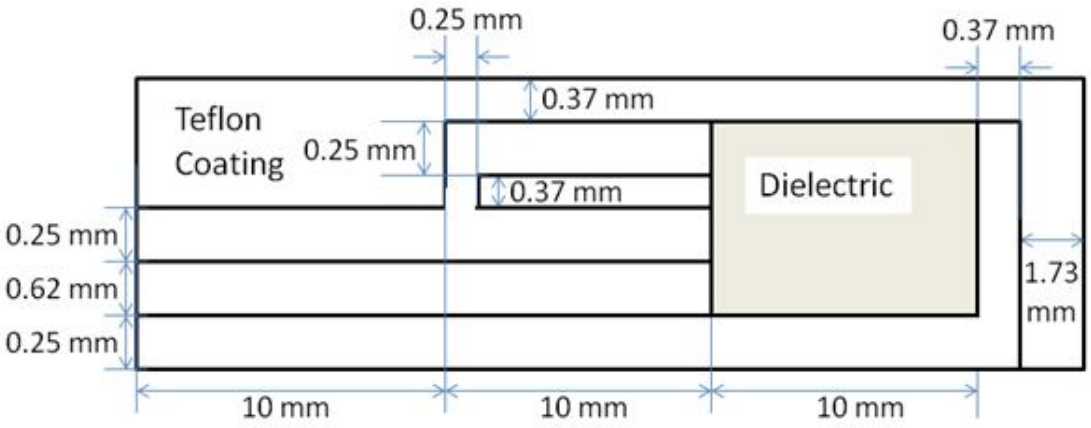

Figure 4.8(a): *Antenna with termination cap, Sleeve choke and Dielectric in blood medium along with dimensions*

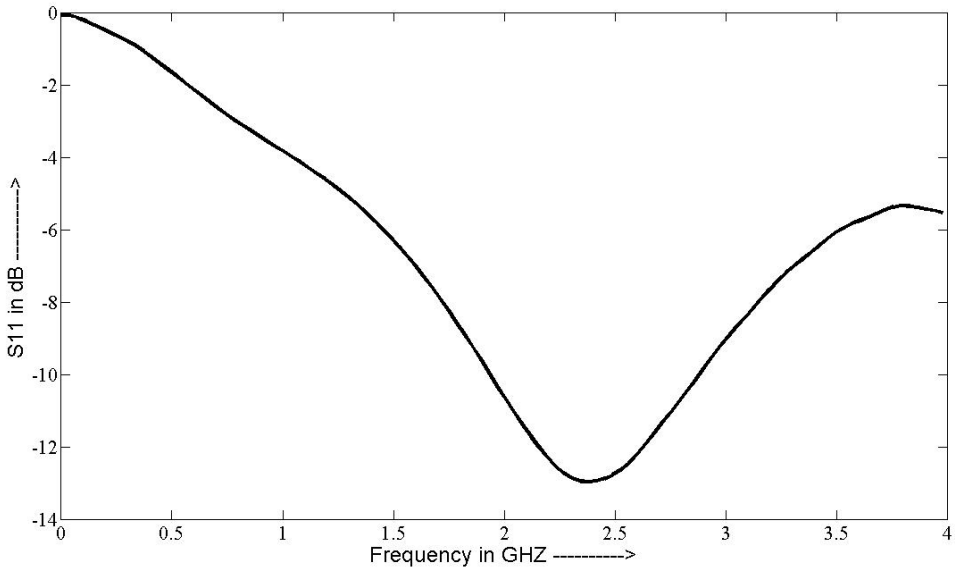

Figure 4.8(b): *S11 for the antenna with termination cap, Sleeve choke and dielectric in blood medium*

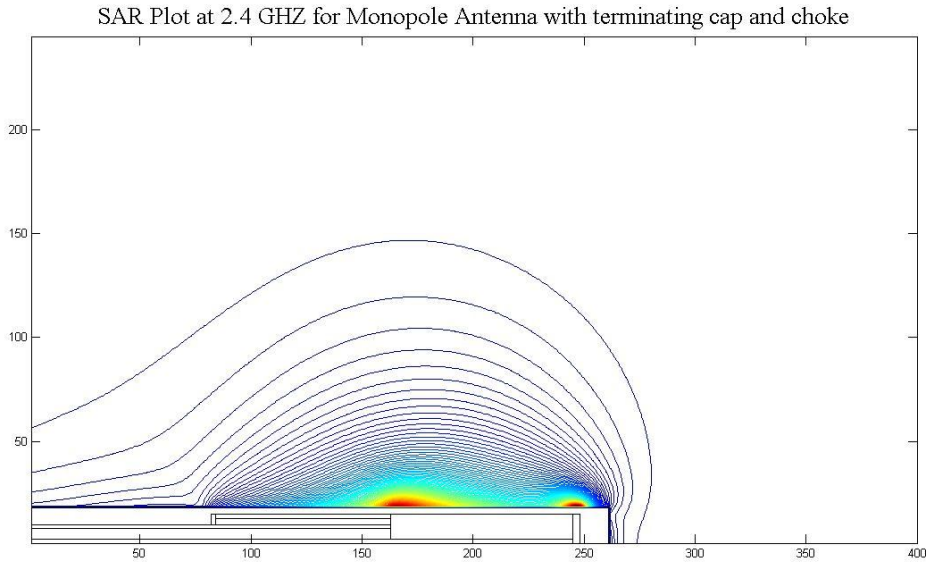

Figure 4.8(c): *SAR profile for the antenna with termination cap, Sleeve choke and dielectric in blood medium*

The monopole with a length of 10.5 mm immersed in Teflon medium should resonate at 2.38 GHz. The 10 dB bandwidth has been found to be 0.95 GHz. The antenna with the dielectric has a wider bandwidth because of better matching between the blood medium and the antenna. The FDTD results match with the published results in [24].

This antenna is immersed in Blood media. Hence Wheelers ESA formulation will not be applicable for this antenna. To overcome this, a new antenna with different dimensions in air medium is designed. The same FDTD code is used for analysis of the structure.

4.5.5 Modified Catheter Antenna as an ESA in Air Medium

The previous antenna design is not an electrically small antenna. Figure 4.9(a) shows the monopole antenna along with the terminating cap and a in air medium. Figure 4.9(b)

shows the S11 parameters of the antenna in both air media for different dielectric constants. The choke was found to be having a dominant effect on the antenna performance. Hence it was removed to prevent it from dominating over the metamaterial coating as the main objective is to study the effects of metamaterial on an ESA.

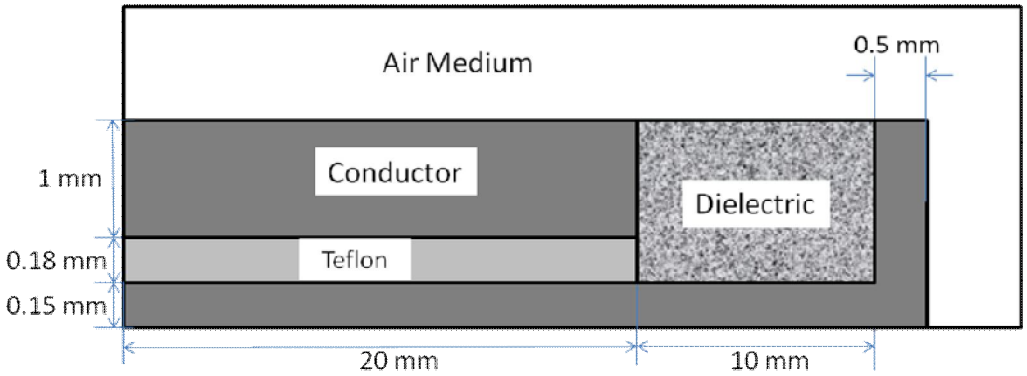

Figure 4.9(a): *Antenna that will be modified as an ESA*

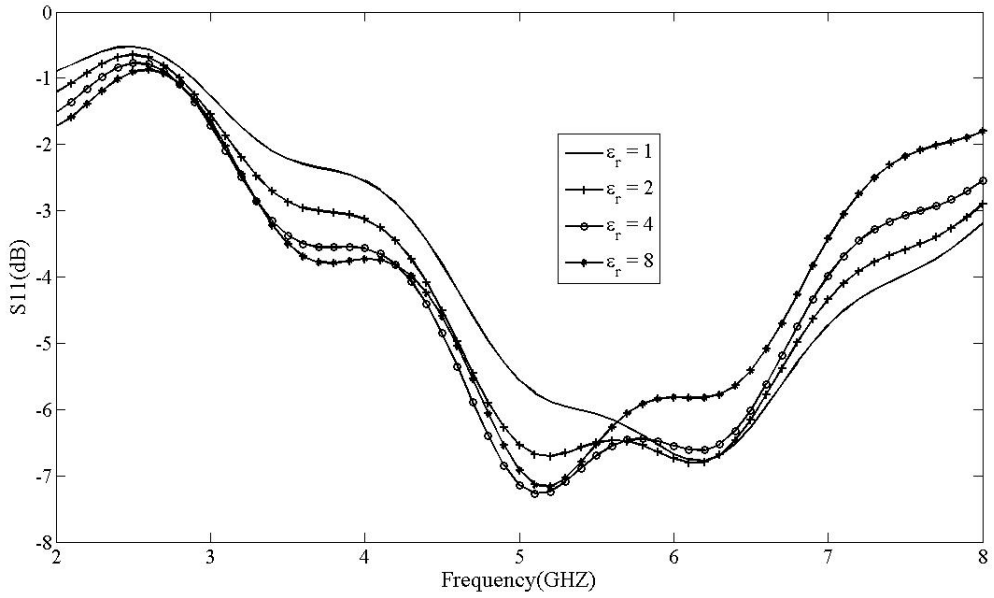

Figure 4.9(b): *S11 for the antenna in air media with different dielectric constants*

The maximum dimension of the antenna is approximately 10.6 mm. The resonant frequency of the antenna is around 5 GHz. The value of *ka* is 0.555 and is therefore an ESA according to Wheelers formulation. The minimum Q factor or the Chu limit from McLean's exact equation for this antenna is 7.65. The Input Impedance of the antenna with a dielectric constant of 2 is shown in figure 4.10. It is clear from the imaginary part of the input impedance that the ESA is highly capacitive in nature. This is also a reason for rather poor S11 characteristics of the antenna in figure 4.9(b).

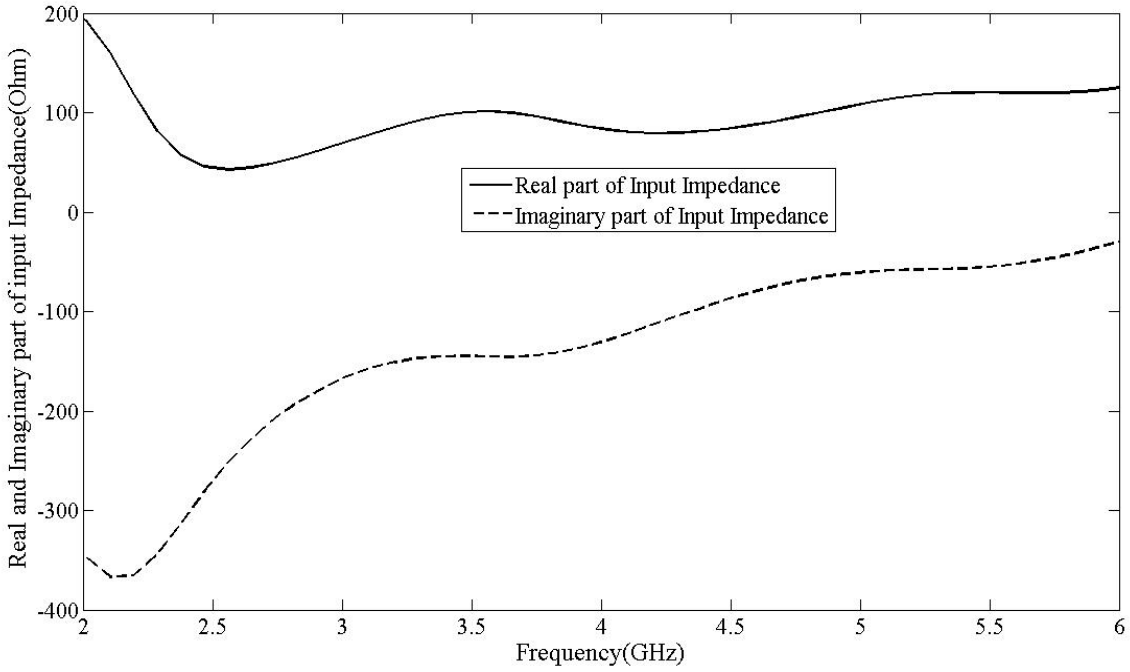

Figure 4.10: *Real and Imaginary parts of Input Impedance for the ESA*

4.6 Summary

In this chapter, fundamental properties of ESA's have been detailed. FDTD formulation of the Cylindrical Catheter Antenna was developed in section 4.4. The simulated results from the FDTD code are in agreement with those in [24]. An ESA is developed from the catheter antenna and its Q factor is calculated. The Q factor obtained was found to be higher than the Chu limit.

CHAPTER V

METAMATERIAL ANTENNA

5.1 Introduction

ESA suffer from very small radiation resistance and high capacitive reactance. To overcome the large impedance mismatch, good matching networks need to be implemented. In the era where every inch of real estate costs, this is certainly not an optimized solution. Metamaterials with their engineered electromagnetic responses have been recently found to be useful in tackling this problem [30-31]. Incorporating Metamaterials into ESA systems can provide a good FBW as well as efficiency.

This chapter provides a paradigm for achieving an efficient ESA. Part of the wrap around dielectric in the antenna in Figure 4.8(a) is replaced with a metamaterial. An FDTD code for cylindrical dispersive metamaterial is formulated. It is then used to discern the different properties of the metamaterial antenna. Use of Epsilon Negative (ENG) metamaterials and Double Negative (DNG) metamaterials is investigated. ESA-metamaterial system is shown to have a Q factor less than the Chu limit.

5.2 Metamaterial for ESA

In Chapter IV we showed an ESA design that was highly capacitive in nature. This design has a very small radiation resistance while simultaneously having a large capacitive reactance. To match such an antenna, a large inductance is required. ENG or DNG Metamaterials with negative permittivity are inductive in nature. Negative

permittivity leads to negative capacitance which is nothing but inductance. When an ESA is placed in a metamaterial medium, they match up to form a LC resonant circuit. This leads to a good match with the input source and hence good efficiency.

The ESA-metamaterial system is characterized using two different quality factors, the transmission line quality factor or Q_{TL} [32] and the half power quality factor or Q_{VSWR} [33]. The Q_{TL} is calculated form -10 dB return loss frequency points as,

$$Q_{TL} = \frac{f_0}{\Delta f_{-10dB}} \tag{5.2.1}$$

The half power quality factor is given by,

$$Q_{VSWR} = \frac{2}{FBW_{-3dB}} \tag{5.2.2}$$

where FBW_{-3dB} is the fractional bandwidth calculated from form -3 dB return loss frequency points. Both these quality factors will be compared with the Chu limit to establish that an ESA-metamaterial system will indeed lead to wider bandwidth and much more efficient antenna systems.

5.3 FDTD for Cylindrical Metamaterial Antenna

5.3.1 Drude Medium

All Realistic LHMs exhibit dispersive properties [34]. To model the dispersive nature of LHMs, permittivity and permeability are expressed as a function of frequency using the Drude model. The Drude model is described by,

$$\varepsilon_r(\omega) = \varepsilon_\infty - \frac{\omega_{ep}^2}{p_1\omega^2 - j\omega\tau_e} \tag{5.3.1.1(a)}$$

$$\mu_r(\omega) = \mu_\infty - \frac{\omega_{em}^2}{p_2\omega^2 - j\omega\tau_m} \qquad (5.3.1.1(b))$$

where ε_∞ is the permittivity at infinite frequency, ω_{ep} is the electric plasma frequency and τ_e is the electric damping factor related to loss. Likewise, μ_∞ is the permeability at infinite frequency, ω_{mp} is the magnetic plasma frequency and τ_m is the magnetic damping factor related to loss. The loss terms τ_e and τ_m are specified as a factor of corresponding plasma frequency.

The parameters p_1 and p_2 are used for coding convenience. They have no significance as far as Drude model is concerned. These constants will allow us to model all kinds of available materials using the same general FDTD code instead of using different code for different materials in the grid. For example if an antenna made of different materials is gridded for FDTD coding, we need to use a different set of FDTD equations to solve for the fields in different media. To solve this p_1 and p_2 are introduced, which can be toggled between 0 or 1 to solve for the fields.

For a lossless dielectric, we set $\varepsilon_\infty = \varepsilon_r$, where ε_r is the dielectric constant of the material, p_1 =1 and $\omega_{ep} = \tau_e$ =0. Equation 5.3.1.1(a) reduces to $\varepsilon_r(\omega) = \varepsilon_\infty$ which represents a lossless dielectric.

For a lossy dielectric Amperes law can be written as,

$$\nabla \times \vec{H} = \sigma \vec{E} + j\omega\varepsilon_0\varepsilon_r \vec{E} = j\omega\varepsilon_0 \vec{E}(\varepsilon_r + \frac{\sigma}{j\omega\varepsilon_0}) \qquad (5.3.1.2)$$

Comparing Equation (5.3.1.1(a)) and (5.3.1.2), for a lossy dielectric, we set $\varepsilon_\infty = \varepsilon_r$, p_1 =0, $\tau_e = \varepsilon_0$ and $\omega_{ep}^2 = \sigma$.

For a perfect electric conductor or a metal, electric and magnetic fields inside the conductor are zero. Hence set all the Drude variables to zero. While coding it is ensured that the denominators are not set to zero.

For a metamaterial, we set ε_∞ =1, $\omega_{ep} = \sqrt{(1+ep)} \times (2\pi f_r)$, where the permittivity is –ep at a frequency f= f_r, p_1 =1 and τ_e depends on loss. τ_e =0 for a lossless case. For ENG metamaterial implementation only the Drude permittivity is set up but in case of DNG metamaterial, both permittivity and permeability are set up.

In case of a lossy metamaterial, we have both real and imaginary values for permittivity and permeability values, whichever is modeled. Figure 5.1 shows the real values for permittivity modeled using equation 5.3.1.1(a) for both lossless as well as lossy case. The Drude model parameters are set such that for a lossless case, the permittivity at 5 Ghz is -9. This is obtained by setting $\omega_{ep} = \sqrt{(1+9)} \times (2 \times \pi \times 5)$ and p_1 =1. It can be observed from the plot as loss increases, the permittivity values get lower and lower.

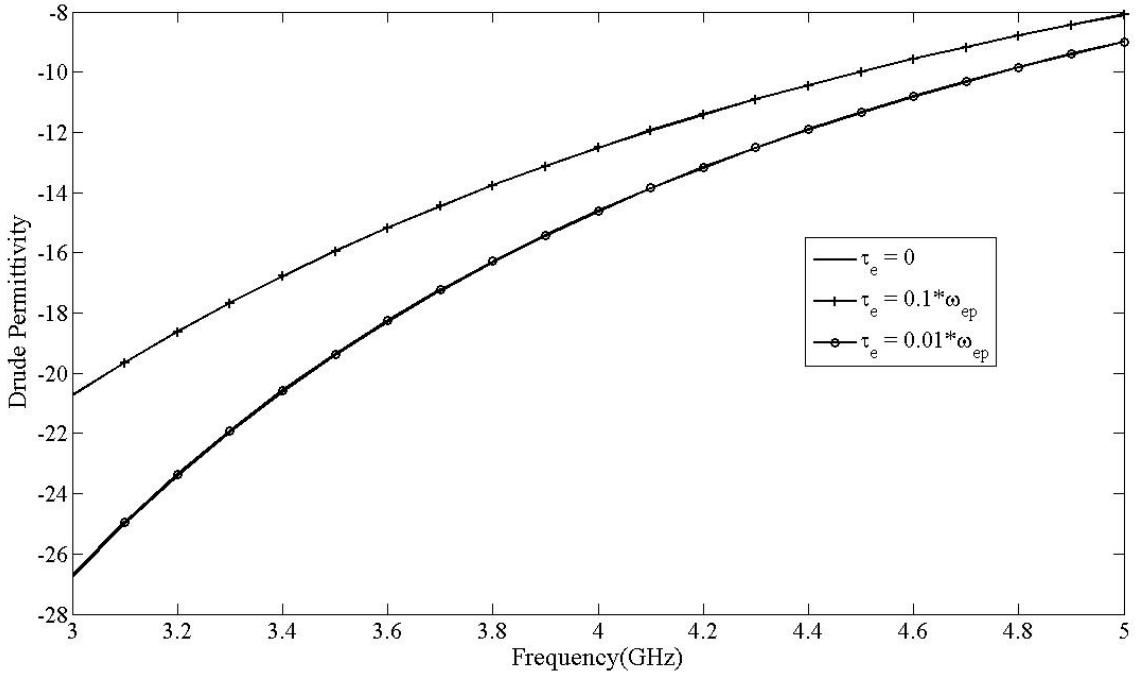

Figure 5.1: *Permittivity values obtained using Drude model*

5.3.2 FDTD Modeling

In Chapter III of the thesis, FDTD implementation of 2D metamaterial structures in Cartesian coordinates has already been discussed. FDTD implementation of cylindrical metamaterial is no different except that the equations have to be redone. There is no need for UPML boundary condition as the metamaterial does not coincide with the boundary in our case. The Lorentz media characterization of dispersive metamaterials as explained in Chapter II is given by,

$$\varepsilon_r(\omega) = \varepsilon_\infty - \frac{\omega_{ep}^2}{p_1\omega^2 - j\omega\tau_e} \qquad (5.3.2.1(a))$$

$$\mu_r(\omega) = \mu_\infty - \frac{\omega_{em}^2}{p_2\omega^2 - j\omega\tau_m} \qquad (5.3.\ 2.1(b))$$

The Maxwell's equation in time domain for the antenna structure are given by,

$$\frac{1}{r}\frac{\partial(rH_\varphi)}{\partial r} = \varepsilon_0 \frac{\partial(E_z\varepsilon_r(\omega))}{\partial t} \qquad (5.3.2.2(a))$$

$$-\frac{\partial(rH_\varphi)}{\partial z} = \varepsilon_0 \frac{\partial(E_r\varepsilon_r(\omega))}{\partial t} \qquad (5.3.2.2(b))$$

$$\frac{\partial(E_r)}{\partial z} - \frac{\partial(E_z)}{\partial r} = -\mu_0 \frac{\partial(H_\varphi\mu_r(\omega))}{\partial t} \qquad (5.3.2.2(c))$$

They are worked upon in steps as in Chapter II. The final equations obtained for implementation of FDTD code are given below.

$$E^{n+1} = \sum_{i=-1}^{1} a_i D^{n+i} + \sum_{i=-1}^{0} b_i E^{n+i} \qquad (5.3.2.3(a))$$

where

$$a_1 = \frac{4p_1 + 2\tau_e\Delta t}{A} \qquad (5.3.2.3(b))$$

$$a_0 = \frac{-8p_1}{A} \qquad (5.3.2.3(c))$$

$$a_{-1} = \frac{4p_1 - 2\tau_e\Delta t}{A} \qquad (5.3.2.3(d))$$

$$b_0 = \frac{8\varepsilon_\infty p_1 - 2\Delta t^2\omega_{ep}^2}{A} \qquad (5.3.2.3(e))$$

$$b_{-1} = \frac{-4\varepsilon_\infty p_1 + 2\varepsilon_0\tau_e\Delta t - \Delta t^2\omega_{ep}^2}{A} \qquad (5.3.2.3(f))$$

$$A = 4\varepsilon_\infty p_1 + 2\varepsilon_0\tau_e\Delta t + \Delta t^2\omega_{ep}^2 \qquad (5.3.2.3(g))$$

The term E in equation (5.3.2.3(a)) refers to both E_z and E_r; D in equation (5.3.2.3(a)) refers to corresponding D_z and D_r.

$$D_z^{n+1}(i,j) = D_z^n(i,j) + \frac{\Delta t}{(j-1)\varepsilon_0 \Delta r}\left(\frac{H_\phi^{n+\frac{1}{2}}(i,j) + H_\phi^{n+\frac{1}{2}}(i,j-1)}{2}\right) + \frac{\Delta t}{\varepsilon_0 \Delta r}\left(H_\phi^{n+\frac{1}{2}}(i,j) - H_\phi^{n+\frac{1}{2}}(i,j-1)\right) \quad (5.3.2.4(a))$$

$$D_r^{n+1}(i,j) = D_r^n(i,j) - \frac{\Delta t}{\varepsilon_0 \Delta z}\left(H_\phi^{n+\frac{1}{2}}(i,j) - H_\phi^{n+\frac{1}{2}}(i,j-1)\right) \quad (5.3.2.4(b))$$

$$H_\phi^{n+\frac{3}{2}}(i,j) = H_\phi^{n+\frac{1}{2}}(i,j) + \frac{\Delta t}{\mu_0 \Delta r}\left(E_z^{n+1}(i+1,j) - E_z^{n+1}(i,j)\right) - \frac{\Delta t}{\mu_0 \Delta r}\left(E_r^{n+1}(i,j+1) - E_r^{n+1}(i,j)\right) \quad (5.3.2.4(c))$$

The iteration procedure can be summed up as in figure 5.1.

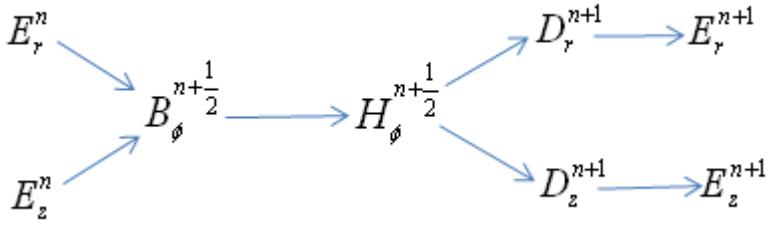

Figure 5.2: *Iteration sequence for the FDTD code*

Figure 5.3 shows the catheter antenna in air medium to be modeled. Cylindrical Liao boundary condition explained in Chapter IV is used to determine the field components on the boundary. At r = 0, the same technique is applied as in Chapter II.

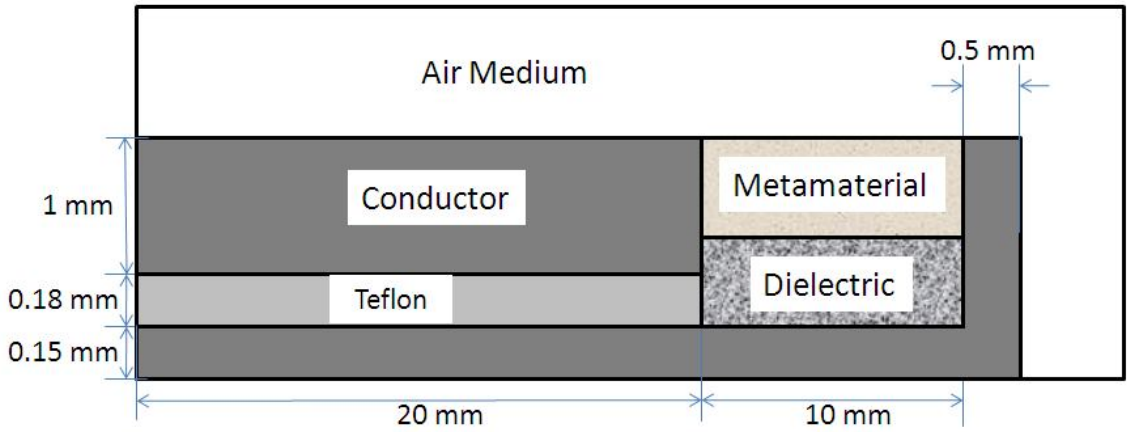

Figure 5.3: *2D view of Antenna to be modeled*

5.4 ENG Metamaterial Wraparound Antenna

ENG or epsilon negative metamaterials are materials which have negative permittivity but positive permeability. A cylindrical ENG wraparound acts as an inductive medium. As discussed earlier, ESA are capacitive in nature. When an ESA radiates in the presence of a properly engineered ENG wraparound, an LC resonator is formed. The resonance frequency depends on the permittivity and the thickness of the ENG wraparound.

Figure 5.4 shows the return loss in dB for varying thickness of the lossless ENG wraparound. The permittivity variation of the ENG wraparound is shown in Figure 5.1 While varying the thickness of the ENG wraparound, the DPS dielectric width is also varied in order to completely fill up the free space in the ESA.

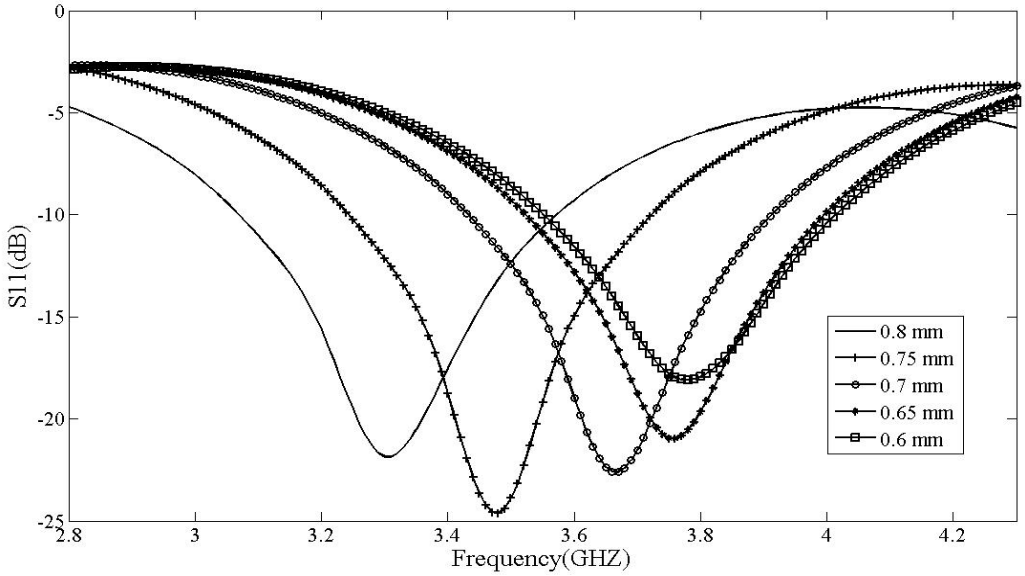

Figure 5.4: *Return loss for an ESA with varying thickness of a lossless ENG*

Table 5.1 summarizes the results obtained by using an ENG wraparound with varying thickness.

Table 5.1: *Results obtained for an ENG wraparound by varying thickness*

Thickness	**Resonant Frequency**	**Ka**	**Q_{chu}**	**FBW**	**Q_{TL}**	**Q_{VSWR}**
0.8 mm	3.22 Ghz	0.3574	24.697	13.98%	7.155	-
0.75 mm	3.481 Ghz	0.3864	19.921	13.72%	7.2977	-
0.7 mm	3.666 Ghz	0.4069	17.297	12.79%	7.8166	5.324
0.65 mm	3.755 Ghz	0.4168	16.208	12.38%	8.0753	5.518
0.6 mm	3.777 Ghz	0.4192	15.948	12.24%	8.19	5.202

From Table 5.1, all the Q_{TL} and Q_{VSWR} values of the ENG-ESA system are less than the Chu limit. It is clear from the table that as the thickness of the ENG wraparound decreases, the Q_{TL} values increases. Q_{VSWR} does not follow the same trend as the Q_{TL} values but compares well with Q_{TL} values obtained. Decrease in ENG wraparound thickness also leads to an increase in the resonant frequency. This can be interpreted as a decrease in the amount of inductance added by the ENG wraparound to the ESA system.

5.5 DNG Metamaterial Wraparound Antenna

DNG or Double negative metamaterials are materials which have negative values of both permittivity and permeability. A cylindrical DNG wraparound adds an inductance as well capacitance to the ESA system. The negative value of permittivity acts as an inductance and the negative value of permeability acts as a capacitance. The resonance frequency depends on the permittivity, permeability and the thickness of the DNG wraparound.

The permittivity and permeability variation of the DNG wraparound is shown in Figure 5.5. Figure 5.6 shows the return loss in dB for varying thickness of the lossless DNG wraparound. While varying the thickness of the DNG wraparound, the DPS dielectric width is also varied in order to completely fill up the free space in the ESA.

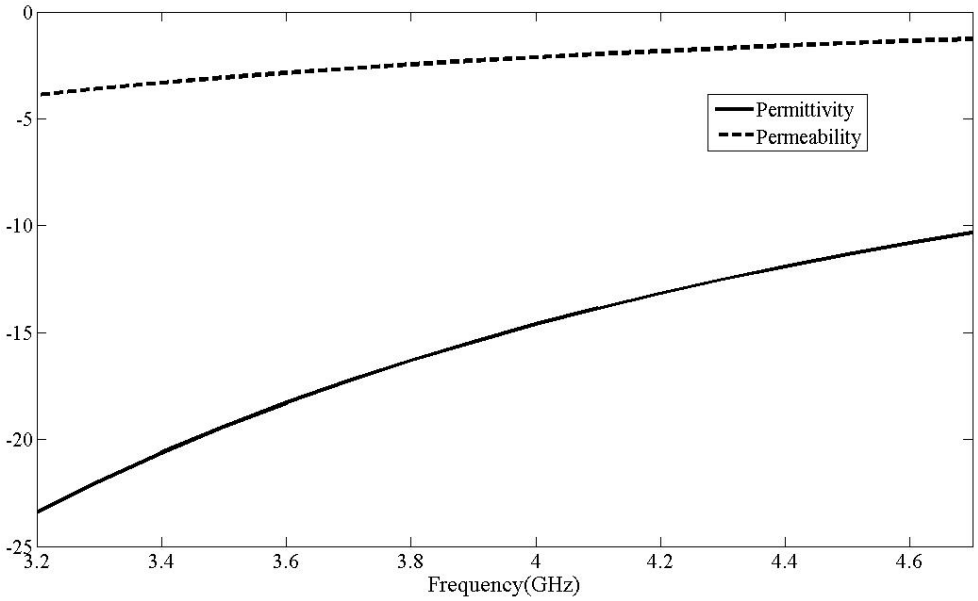

Figure 5.5: *Permeability and Permittivity variation for a DNG metamaterial*

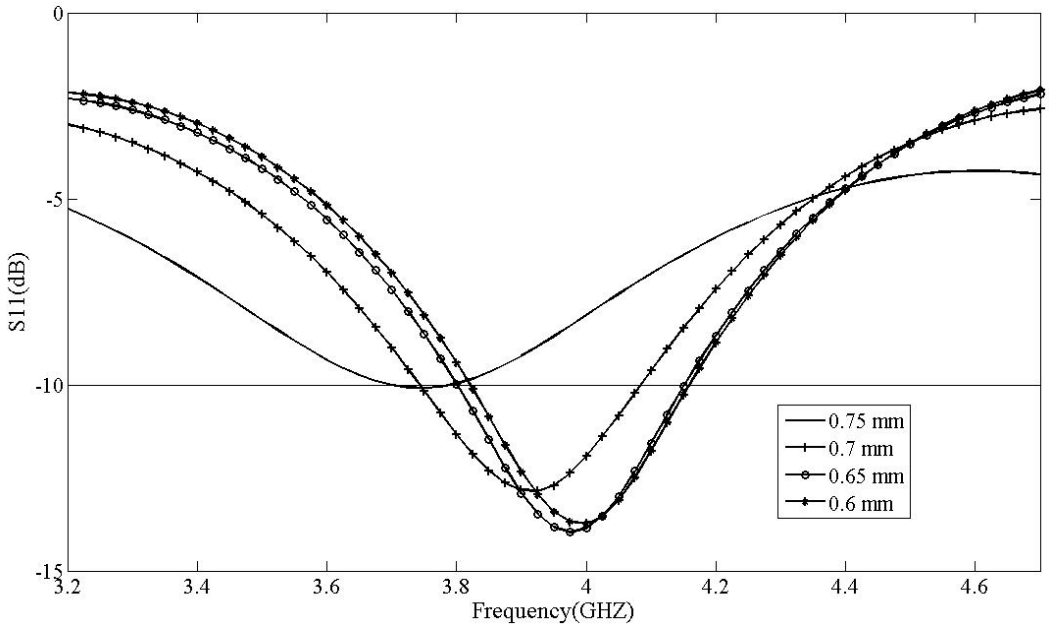

Figure 5.6: *Return loss for an ESA with varying thickness of a lossless DNG metamaterial*

Table 5.2 summarizes the results obtained by using a DNG wraparound with varying thickness.

Table 5.2: *Results obtained for an DNG wraparound by varying thickness*

Thickness	**Resonant Frequency**	**Ka**	**Q_{chu}**	**FBW**	**Q_{TL}**	**Q_{VSWR}**
0.75 mm	3.745 Ghz	0.415	16.32	2.48%	40.269	-
0.7 mm	3.916 Ghz	0.434	14.475	8.7%	11.484	5.688
0.65 mm	3.976 Ghz	0.441	13.89	8.82%	11.334	6.68
0.6 mm	3.993 Ghz	0.443	13.74	8.48%	11.767	6.95

From Table 5.2, all the Q_{TL} and Q_{VSWR} values of the ENG-ESA system are less than the Chu limit except for the case with a thickness of 0.75 mm. This can be attributed to improper DNG metamaterial engineering. It is clear from the table that as the thickness of the DNG wraparound decreases, the Q_{TL} values increases. Q_{VSWR} follows the same trend as the Q_{TL} values and compares well with Q_{TL} values obtained. Decrease in DNG wraparound thickness also leads to an increase in the resonant frequency. This can be interpreted as a decrease in the amount of inductance added by the ENG wraparound to the ESA system.

5.6 Summary

In this chapter, FDTD formulation of the Metamaterial Catheter Antenna was developed. The simulated results from the FDTD code are presented in section 5.3 and 5.4. The

ESA is used in conjunction with both ENG and DNG wraparounds and the Q factor is calculated in both the cases. The Q factors obtained are found to be significantly lower than the Chu limits thus validating the claim that an ESA-metamaterial syetm when properly engineered can provide much higher bandwidths than theoretically permissible limits.

CHAPTER VI

CONCLUSIONS

6.1 Summary

This thesis presented a new paradigm for ESA by combining a coax fed modified catheter antenna and a cylindrical metamaterial. It was shown that a properly engineered configuration of metamaterial and ESA is capable of much lower resonant frequency when compared with its free space counterpart. The inductive nature of metamaterials with negative permittivity compensates the highly capacitive ESA. This combination forms a LC tank to provide a good resonance. This thesis included metamaterials with dispersion characteristics as well as loss modeled using a Drude model.

An ADE FDTD code was developed to model the antenna and discern its characteristics. The metamaterials used were both DNG and ENG in nature. For the same dispersion characteristics used, the ENG metamaterials were found to have a lower resonant frequency when compared with its DNG characteristics. The metamaterial ESA system when engineered properly was found to have higher bandwidths and lower quality factors than the Chu limit without any degradation of radiation patterns of the constituent antenna.

REFERENCES

[1] K.S. Yee, “Numerical solution of intitial boundary value problems involving maxwell’s equations in isotropic media," *IEEE Transactions on Antennas and Propagation*, vol. AP-14, pp. 302-307, May 1966.

[2] A. Taflove and S. C. Hagness, *Computational Electrodynamics: The Finite Difference Time Domain Method*, 3rd ed. Norwood, MA: Artech House, 2005.

[3] B. Engquist and A. Majda, “Absorbing boundary conditions for the numerical simulation of waves,” *Mathematics of Computation*, vol. 31, pp. 629-651, Jul. 1977.

[4] G. Mur, “Absorbing boundary conditions for the finite difference approximation of the time domain electromagnetic field equations," *IEEE Transactions Electromagn. Compat.*, vol. 23, pp. 377-382, Nov. 1981.

[5] Z. P. Liao, H. L. Wong, B. P. Yang, and Y. F. Yuan, “A transmitting boundary for transient wave analyses,” *Scientia Sinica* (series A), vol. XXV11, pp. 1063-1076, 1984.

[6] S. D. Gedney, “An anisotropic perfectly matched layer-absorbing medium for the truncation of FDTD lattices," *IEEE Transactions on Antennas and Propagation*, vol. 44, no. 12, pp. 1630-1638, Dec. 1996.

[7] D. R. Smith, W. J. Padilla, D. C. Vier, S. C. Nemat-Nasser, and S. Schultz, “Composite media with simultaneously negative permeability and permittivity," *Physical Review Letters*, vol. 84, no.18, pp. 4184-4187, May 2000.

[8] J. B. Pendry, “Negative refraction," *Contemporary Physics*, vol. 45, no.3, pp. 191-202, Jan-Feb 2004.

[9] V. Veselago, “The electrodynamics of substances with simultaneously negative values of ε and μ,” *Sov. Phys. Usp.*, vol. 10, no.4, pp. 509-514, Jan-Feb 1968.

[10] J. B. Pendry, “Negative refraction makes a perfect lens,” *Physical Review Letters*, vol. 85, pp. 3966-3969, Oct. 2000.

[11] M. A. Antoniades and G. V. Eleftheriades, “Compact linear lead/lag metamaterial phase shifters for broadband applications,” *IEEE Antennas and Wireless Propagation Letters*, vol. 2, pp. 103-106, Jul. 2003.

[12] J. B. Pendry, “Manipulating the near field with metamaterials,” *Optics and Photonic News*, vol. 15, pp. 33-37, Sep. 2004.

[13] D. R. Smith, J. B. Pendry, and M. Wiltshire, “Manipulating the near field with metamaterials,” *Science*, vol. 305, pp. 788-792, Aug. 2004.

[14] P. Markos and C. M. Soukoulis, “Numerical studies of left-handed materials and arrays of split ring resonators,” *Physical Review E*, vol. 65, p. 036622, Mar. 2002.

[15] P. Kolinko and D. R. Smith, “Numerical study of electromagnetic waves interacting with negative index materials,” *Optics Express*, vol. 11, no.7, pp. 640-648, Apr. 2003.

[16] M. Kafesaki, T. Koschny, R. Penciu, T. Gundogdu, E. Economou, and C. M. Soukoulis, “A numerical study of evanescent fields in backward-wave slabs,” *Journal of Optics A: Pure and Applied Optics*, vol. 7, pp. S12-S22, Feb. 2005.

[17] A. Tafove and S. C. Hagness, *Computational Electrodynamics: The Finite Difference Time-Domain Method,* 2nd ed. Boston: Artech House, 2000.

[18] R. A. Shelby, D. R. Smith, S. Nemat-Nasser, and S. Schultz, "Microwave transmission through a two dimensional, isotropic, left-handed metamaterial," *Applied Physics Letters*, vol. 78, no.4, pp. 489-491, Jan. 2001.

[19] R. W. Ziolkowski, "Pulsed and CW Gaussian beam interactions with double negative metamaterial slabs," *Opt Express* vol. 11, pp. 662–681, Apr. 2003.

[20] R. J. Luebbers, F. Hunsberger, K. S. Kunz, R. B. Standler, and M. Schneider, "A frequency dependent finite difference time-domain formulation for dispersive materials," *IEEE Transactions on Electromagnetic Compatibility*, vol. 32, pp. 222-227, Aug. 1990.

[21] O. P. Gandhi, B. Q. Gao, and J. Y. Chen, "A frequency-dependent finite difference time domain formulation for general dispersive media," *IEEE Transactions on Microwave Theory and Techniques*, vol. 41, pp. 658-664, Apr. 1993.

[22] D. M. Sullivan, "Frequency-dependent FDTD methods using z transforms," *IEEE Transactions on Antennas and Propagation*, vol. 40, pp. 1223-1230, Oct. 1992.

[23] S. A. Cummer, "Perfectly matched layer behavior in negative refractive index metamaterials," *IEEE Antennas and Wireless Propagation Letters*, vol. 3, pp. 172-175, Jul. 2004.

[24] R. D. Nevels, G. Dickey, W. Raffoul, J. R. Carl, and A. Pacifico, “Microwave catheter design," *IEEE Transactions on Biomedical Engineering*, vol. 45, no. 7, pp. 885-890, May 1998.

[25] H. A. Wheeler, “Fundamental limitations of small antennas," *IRE Proc.*, vol. 35, pp. 1479-1484, Dec. 1947.

[26] L. J. Chu, “Physical limitations of omnidirectional antennas," *J.Appl. Phys*, vol. 19, pp. 1163-1175, May 1948.

[27] J. S. Mclean, “A re-examination of the fundamental limits on the radiation Q of electrically small antennas," *IEEE Transactions on Antennas and Propagations*, vol. 44, No. 5, pp. 672-675, May 1996.

[28] J. G. Maloney, G. S. Smith, and W. R. Scott, “Accurate computation of the radiation from simple antennas using finite-difference time-domain method," *IEEE Transactions on Antennas and Propagations*, vol. 38, no. 7, pp. 1059-1068, May 1990.

[29] Z. P. Liao, H. L. Wong, B. Yang, and Y. Yuan, “A transmitting boundary for transient wave analysis," *Sci. Sin., Ser. A,* vol. 27, pp. 1063-1076, May 1984.

[30] R. W. Ziolkowski and A. Erentok, “Metamaterial based efficient electrically small Antennas,” *IEEE Trans. Antenna Propagat.* vol. 54, no. 7, Jul. 2006.

[31] N. Enghata and R. W. Ziolkowski, “A positive future for double negative meta-materials,” *IEEE Microwave Theory Tech.,* vol. 53, no. 4, pp. 1535-1556, Apr. 2005.

[32] R. W. Ziolkowski, "A discussion on the quality factor of impedance matched electrically small wire antennas," *IEEE Trans. Antenna Propagat.* vol. 53, no. 1, pp. 502-508, Jan. 2005.

[33] C. A. Balanis, *Antenna Theory*, *3rd ed.* New York: Wiley, 2005.

[34] R. W. Ziolkowski and A. Kipple, "Causality and double-negative metamaterials," *Phys. Rev. E*, vol. 68, 0226615, Aug. 29, 2003.

VITA

Vipin Krishna Reddy Cholleti obtained his Bachelor of Technology degree in electronics and communication engineering from Indian Institute of Technology, Guwahati in May 2007. He can be reached at: Department of Electrical and Computer Engineering, Texas A&M University, 214 Zachry Engineering Center, TAMU 3128, College Station, Texas 77843-3128. His email is cholleti@neo.tamu.edu.